

Study of Double Parton Scattering in four lepton
events in pp collisions at $\sqrt{s} = 13$ TeV with the
ATLAS detector at the LHC

Moshe Barboy

July 2020

Abstract

Estimation of the number of Double Parton Scattering (DPS) events with 4-lepton final state, in 80fb^{-1} inclusive luminosity that was collected by the ATLAS detector of proton-proton collisions at center-of-mass energy of 13 TeV at the LHC. Out of 3363 events selected in the analysis, a fraction of 0.019 ± 0.0084 was found to be DPS. The found fraction leads to an estimate of the protons overlapping area of $\sigma_{eff} = 6.3 \pm 2.9 \text{ mb}$. These results show that DPS processes are not negligible and can constitute a significant background for measurements done in the 4 lepton channel. The methods used to estimate the fraction were used in previous studies of the process.

Acknowledgements

This work was done under the supervision of Professor Halina Abramovich and with the help of Doctor Oleg Kuprash.

The analysis was done in the ATLAS collaboration. I got a lot of help from various ATLAS teams. A big part of the analysis was implemented by a software received from the ATLAS HZZ group.

Thanks a lot to my friends and family who greatly supported me during the writing.

I am also thankful to the secretariat and education committee in Tel Aviv University, without which I would probably never have had the chance to submit this work.

Contents

1	Introduction	6
2	Introduction to Double Parton Scattering	9
2.1	Proton-Proton Collisions	9
2.2	DPS Definition and σ_{eff}	10
2.3	Four Lepton Channel	12
3	Experiment	16
3.1	Triggers	17
4	Event Samples	19
4.1	Data	19
4.2	Monte Carlo Samples Introduction	19
4.3	Produced MC Samples	21
5	Selection	24
5.1	Selection	24
5.2	DPS Construction	27
6	Background and Uncertainties	29
6.1	Correction to MC	29
6.2	Estimation of Misidentified and Prompt Leptons	30
6.3	Overall Scale	32
6.4	Uncertainties	32
6.5	Control Plots	33

7	Methodology of DPS Fraction Extraction	40
7.1	Discriminating Variables	40
7.2	DPS Estimation Method	45
7.3	Signal Extraction	49
7.4	Sigma Effective	50
8	Results and Conclusions	52
8.1	Conclusions	56
	Appendices	57
A	Map of MC Processes to ATLAS Names	58
B	Detector Calibration Systematic Uncertainties	61

Chapter 1

Introduction

The standard model of fundamental constituents of matter and their interaction (SM) was completed by the discovery of the Higgs boson of mass 125 GeV. It was discovered in proton-proton interaction at the Large Hadron Collider (LHC) in 2012 at center of mass energy of 8 TeV [1, 2]. Since then no further discoveries, which would indicate a hint of physics beyond the SM, were made. Precision measurements of the properties of the Higgs boson thus became a central theme of the research program in the LHC. The presence of the Higgs boson in LHC can be inferred from either by observing a resonant state or by observing an excess of events over the SM without the Higgs. Both of these measurements are possible for any final state that the Higgs can decay to. The expected branching ratios of Higgs decays as a function of its mass are presented in Figure 1.1. The channels with the highest branching ratios are not the

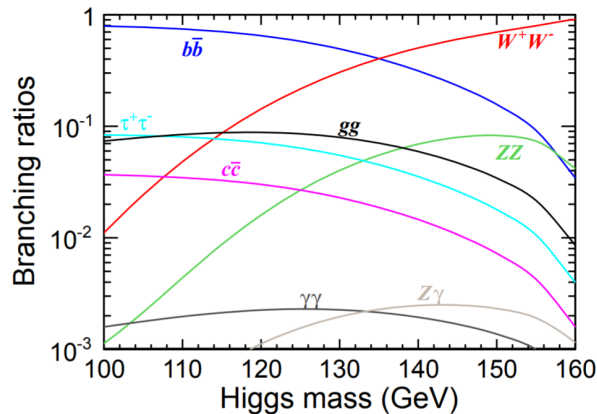


Figure 1.1: Branching ratios of the Standard Model Higgs as a function of the Higgs mass [3].

easiest to explore experimentally in particular, as far as the properties of the Higgs boson are concerned. The best channel to determine the invariant mass and spin of the Higgs is the one in which the Higgs couples to two Z bosons. One of the Z bosons is off-shell and further denoted by Z^* . Each of the Z bosons subsequently decay into two same-flavour-opposite-charged leptons. The charged leptons referenced throughout the text are either electrons or muons (electrons and muons will be denoted with l). Tau leptons decay too fast to be easily measured. Neutrino are only interacting through the weak force and are very hard to measure as well. The well measured decay channels of ZZ^* are therefore: $4e$, 4μ , $2e2\mu$. For short, these channels are referred to as $Z \rightarrow 4l$. The channel $H \rightarrow ZZ^* \rightarrow 4l$ is called the "golden channel" for measuring the Higgs properties. The two general purpose detectors at LHC, ATLAS and CMS [4, 5], were designed such that the leptons are well measured. Furthermore, the Higgs production mechanisms that may result in four lepton final state has relatively small background processes, which might mask the measurement or increase its uncertainty.

The proton is not an elementary particle and its partonic nature makes the proton-proton collisions complicated even if the interaction is hard and only involves partons. It also makes it possible for multiple hard parton interactions (MPI) to occur in a single proton-proton collision [6, 7, 8]. A two lepton final state can be produced by a Drell Yan (DY) process, where a quark from one proton annihilates with an anti-quark from another proton into a γ/Z^* that then decays leptonically [9]. In the four lepton channel the most common process of MPI is an occurrence of double DY (DDY), where the DY process happens twice in single proton-proton collision [10]. Following a simplified model of double parton scattering (DPS), which assumes two independent single parton scatterings (SPS), the expectation for DPS in the Higgs measurements is of order of 1% depending on the selected events [11]. However, most of the measurements of the DPS cross section, on which this prediction is based, were performed in channels dominated by gluon initiated processes. In the four lepton channel, quark and anti-quark initiated processes have a bigger contribution than gluon initiated processes, and if the DPS mechanism is not universal for all partons, might significantly contribute to the Higgs background [12, 13]. Therefore, it was essential to independently estimate the DPS cross section in the four lepton channel, in order to determine its contribution in the Higgs measurements. The ATLAS collaboration published the

measurements of inclusive four lepton production in pp interactions at 8 TeV [14] and at 13 TeV [15]. A study that estimates the amount of events that potentially originates from DPS was published only for 8 TeV [11]. Its results showed no significant contribution of DPS. Consequently, an upper limit of 3% was estimated for the DPS fraction in the selected sample of the $4l$ channel.

The study presented in this thesis is based on large statistics data sample collected during 2015-2017, which constitutes about 58% of all collected data in the second running period of LHC (Run 2). The study follows the 8 TeV DPS study and estimates the amount of DPS at 13 TeV. The analysis at 13 TeV is motivated by a possible increase in DPS due to the bigger flux of partons for low values of proton momentum fractions at higher collision energies.

This work is organized as follows: Chapter 2 introduces the treatment of DPS in hadron-hadron collisions. The definition of the process and its historical measurements are presented there together with the motivation for measuring DPS in the four lepton channel. It also summarises the measurements of the so called effective cross section, σ_{eff} . Chapter 3 describes the experimental environment. Chapter 4 describes the data and simulation samples used for the study. It also has a short introduction to the role of the simulation in the experiment. Chapter 5 describes the data selection, and the method for simulating the DPS process. Chapter 6 describes methods used to improve the simulation and estimate the uncertainties of the simulated samples. Chapter 7 describes the methodology of DPS estimation. Chapter 8 presents the results and conclusions of the study.

Chapter 2

Introduction to Double Parton Scattering

2.1 Proton-Proton Collisions

The SM provides cross section expectations only for processes with elementary particles in the initial state. In high energy collisions the proton consists of many partons. Due to the composition nature of protons, a summation over all possible initial states needs to be performed to determine the cross section for a given final state. Usually it is assumed that only one parton from each colliding proton participates in the interaction that produces the final state. This case is specified as Single Parton Scattering (SPS). For a given final state f , the cross section is given by

$$\sigma_{SPS}(pp \rightarrow f + X) = \sum_{ij} \int dx_1 dx_2 F_i(x_1, Q) F_j(x_2, Q) \hat{\sigma}_{i+j \rightarrow f}(x_1, x_2, Q) \quad (2.1)$$

Here the sum was over the partons in each proton, that can produce the final state; x_1, x_2 are the momentum fractions of the proton carried by the interacting partons; F_i is the probability distribution function (PDF); Q is the interaction scale that is usually of the same order as the center of mass energy \sqrt{s} of the interaction; $\hat{\sigma}$ is the parton cross section that is calculated by the SM and X presents the debris of the protons after the collision. For mass-less partons and protons with momentum P , $\sqrt{s} = \sqrt{4x_1x_2P^2}$.

The PDF provides the probability to find a parton in a proton with momentum fraction x . It is determined from a fit to a wide range of deep inelastic and related hard scattering data [16]. The basic procedure is to parametrize the PDF for a low value

of Q , and then calculate it at higher Q by evolution equations. The PDF fits that were implemented in this study were mostly CT10 [17] and NNPDF30NNLO [18]. Figure 2.1 shows the CT10 fit for different Q values.

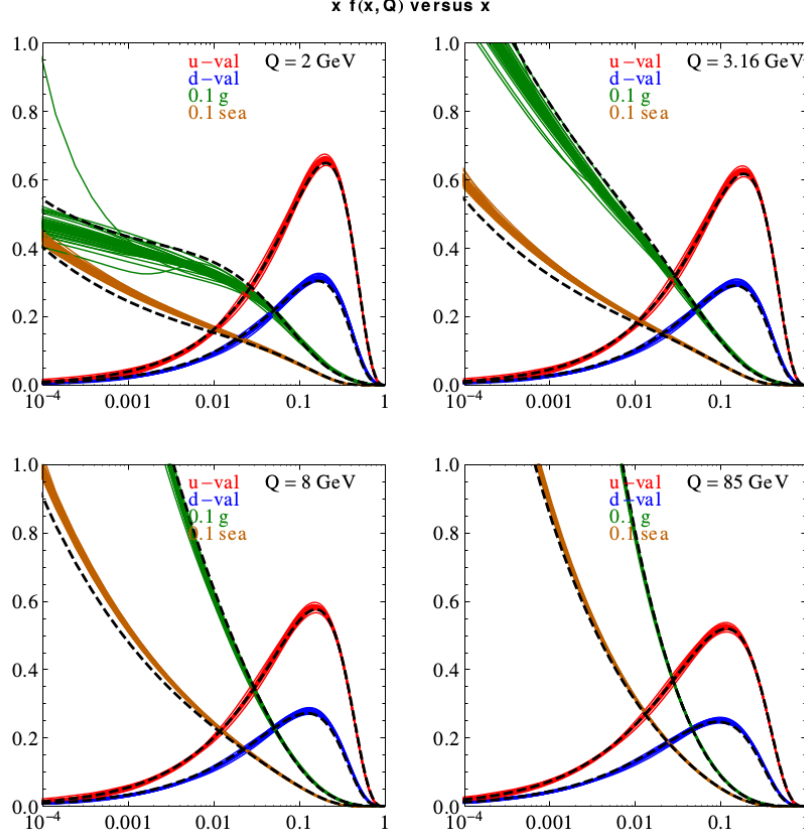


Figure 2.1: CT10 NNLO PDFs. These figures show a central fit, with dashed curve, and additional 50 alternate fits that were produced using the Hessian method. Each graph shows $xu_{valence} = x(u - \bar{u})$, $xd_{valence} = x(d - \bar{d})$, $0.1g$ and $0.1q_{sea}$ as functions of x for a fixed value of Q . The values of Q are 2, 3.16, 8, 85 GeV. The quark sea contribution is $q_{sea} = 2(d + u + s)$. Figures were taken from [17].

2.2 DPS Definition and σ_{eff}

The PDF shows a rise in the number of gluons and sea quarks for low values of x . The rise becomes even more apparent, the higher the value of Q . Due to the large flux of particles in the proton it is possible to have multiple hard parton interaction (MPI) in a single proton-proton collision. Furthermore, for a given final state, more energetic collisions lead to larger cross section expectations for MPI contributions.

Double Parton Scattering (DPS) is a particular case of MPI where, in a single collision, four partons participate in two distinct two-parton interactions. In the case of DPS, the theoretical prediction, similarly to (2.1), is given by

$$\sigma_{DPS}(pp \rightarrow f + X) = \sum_{ijkl} \int dx_1 dx_2 dy_1 dy_2 d^2 b_T G_{ij}(x_1, x_2, b_T, Q_1, Q_2) \hat{\sigma}_{ik}^A(x_1, y_1, Q_1) \hat{\sigma}_{jl}^B(x_2, y_2, Q_2) G_{kl}(y_1, y_2, b_T, Q_1, Q_2) \quad (2.2)$$

Here the sum is over all parton combinations in the colliding protons, that can produce the desired final state; x_1, x_2, y_1, y_2 are the momentum fractions of the interacting partons; G_{ij} is a double parton distribution function (dPDF), which depends on the impact parameter b_T , between the interactions; $\hat{\sigma}^A, \hat{\sigma}^B$ are the parton cross sections for the two disconnected SPS sub-processes, whose combined final state is f . Differently to the SPS case, the integration over the impact parameter b_T , is explicit.

In order to simplify equation (2.2), it is popular to define σ_{eff} as the ratio of the dPDFs and the PDFs. This way all the dependencies between the partons in the proton are contained in one variable:

$$\frac{1}{\sigma_{eff}} \equiv \sum_{ijkl} \int d^2 b_T \frac{G_{ij}(x_1, x_2, b_T, Q_1, Q_2) G_{kl}(y_1, y_2, b_T, Q_1, Q_2)}{F_i(x_1, Q_1) F_j(x_2, Q_2) F_k(y_1, Q_1) F_l(y_2, Q_2)} \quad (2.3)$$

Under the assumption that the dPDF factorizes into two PDFs and a transverse matter distribution function for the integration, σ_{eff} becomes a constant, and equations (2.2) and (2.3) give a simplified relation between the DPS cross section and the SPS cross sections of its sub-processes:

$$\sigma_{DPS} = \frac{1}{1 + \delta} \frac{\sigma_{SPS}^A \sigma_{SPS}^B}{\sigma_{eff}} \quad (2.4)$$

Equation (2.4) is called the "pocket" formula. The combinatorical factor δ is 1 for indistinguishable SPS sub-processes and 0 otherwise. It compensates for double counting in the integral in equation (2.2).

Figure 2.2 shows past measurements of σ_{eff} . The value of σ_{eff} in equation (2.4) was expected to be similar to the cross section of the proton due to its interpretation as the transverse size of the area in which the partons are distributed inside the proton. However, past estimation of it gave much smaller values. The measurements in figure 2.2 indicate a typical value of $\sigma_{eff} = 15$ mb. There are several measurements with lower σ_{eff} , which were done in channels dominated by $q\bar{q}$ initiated interactions, which strengthen the possibility of DPS being non-universal for all the parton combinations.

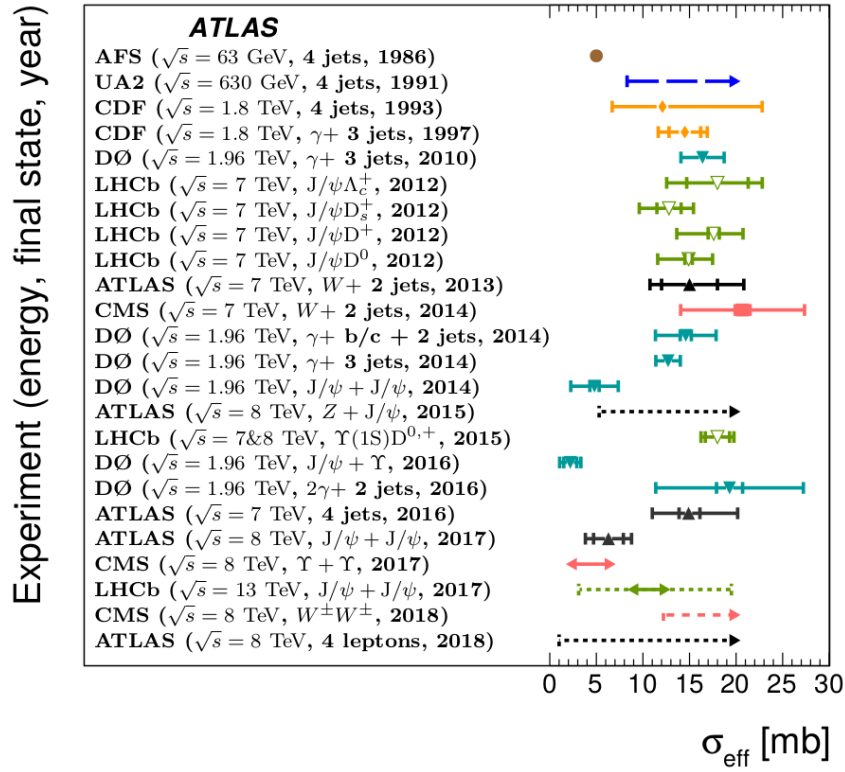


Figure 2.2: σ_{eff} measurements. Plot from [11]

2.3 Four Lepton Channel

The four lepton channel is the choice of taking only events with a final state of at least four leptons, either muons or electrons. When events in the four lepton channel are presented in a histogram categorized by some variable, all possible parton interactions have some contribution to it. The leading order (LO) Feynman diagrams of the most probable processes that can lead to a final state consisting of four leptons in high energy pp collisions are shown in figure 2.3. The diagram of production through a quark-box (gg) is of a higher order than quark-quark (qq) or gluon-quark (gq), but it still has a dominant contribution because of the large gluon flux in low values of x .

Another possibility to get four leptons in the final state is via Higgs production and its subsequent decay to $Z^{(*)}$ bosons and to leptons. The LO of Higgs production diagrams are shown in figure 2.4. The four lepton channel is the golden channel for measuring the Higgs properties. The signal-to-background ratio in this channel is low compared to other decay channels. Moreover, all the components of the Higgs decay are measured, which enables to fully reconstruct its 4-vector. Consequently, the four

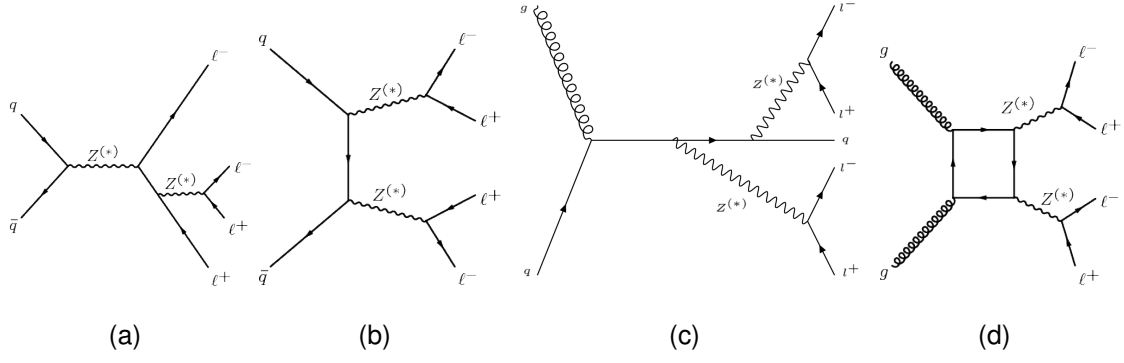


Figure 2.3: Schematic diagrams of processes contribution to the production of four charged lepton in the final state: (a) $q\bar{q}$ production where one of the bosons was produced by associated radiation; (b) $q\bar{q}$ annihilation into two bosons; (c) qg initiated production with another quark in the final state; (d) gg initiated interaction through a quark-box. Taken from [14].

lepton channel played an important role in the Higgs discovery in 2012 [1].

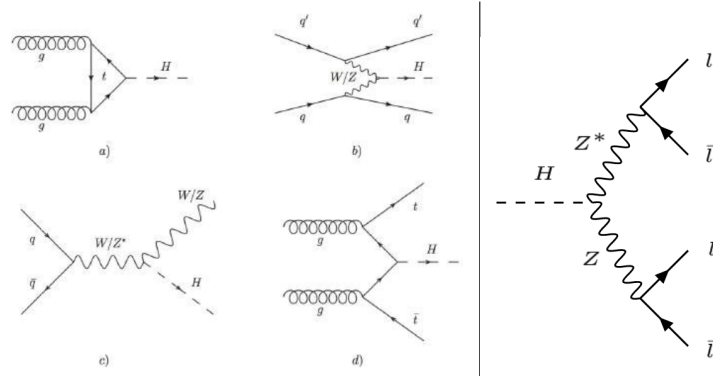


Figure 2.4: Schematic diagrams of Higgs production and subsequent decay into four charged leptons: (a) gluon-gluon Fusion (ggF); (b) Vector Boson Fusion (VBF); (c) associated production with vector boson (VH); (d) associated production with $t\bar{t}$ (ttH). The Higgs decays leptonically via on-shell (Z) and off-shell (Z^*) bosons. Higgs production diagrams were taken from [19].

The main contribution of DPS in the four lepton channel is coming from occurrences of two Drell Yan (DY) processes, or double DY (DDY). Figure 2.5 shows the contribution of DDY compared to the Higgs contribution in the invariant four lepton mass (m_{4l}) distribution from the DPS search analysis at 8 TeV. The right peak of the DDY is in the vicinity of double Z mass, where the two Z boson are on-shell. The peak in the Higgs mass vicinity occurs artificially because of the combination of the DDY divergence in

low masses and the cuts done in the analysis. This shape of the DDY made it a possible background or even imitator of the Higgs in the early stages of the analysis in LHC [12, 13]. The estimated shape of DPS was similar, but the cross section was unknown and in an extreme scenario could explain the peak of the Higgs, as shown in Figure 2.6. Fortunately, the estimated magnitude of the DPS contribution in the four lepton channel at 8 TeV was negligible. However, estimation of the DPS for the 13 TeV experiment is still important because of the increasing particle flux in the low x region of the PDF that can result in bigger DPS cross section. Moreover, future experiments in High Luminosity LHC might plan on measuring Higgs samples with lower uncertainty on the purity. For achieving better purity, having a small contribution of DPS below the 3% upper limit can be critical.

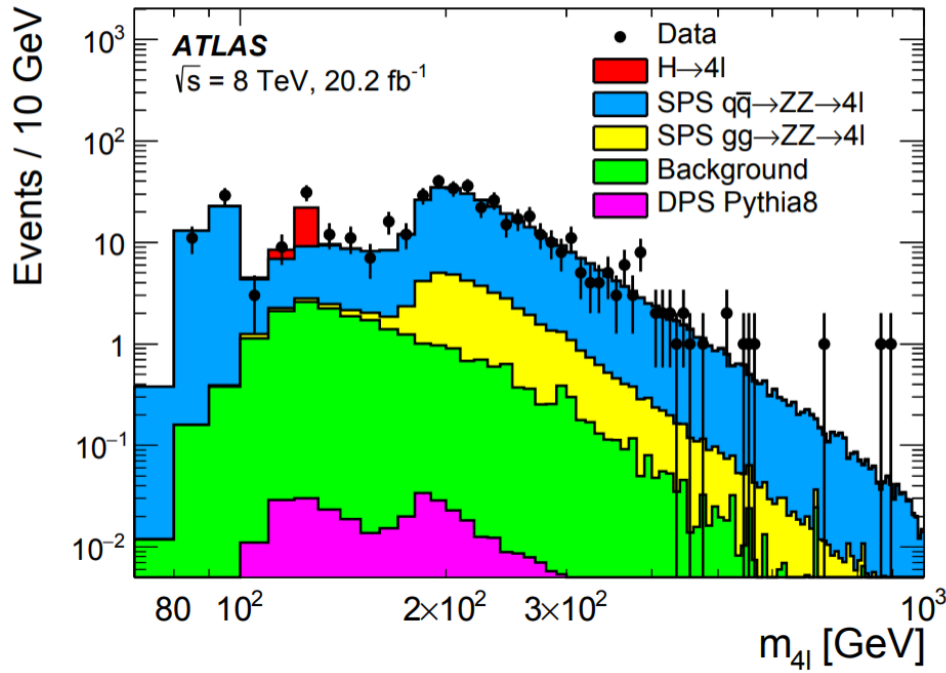


Figure 2.5: Invariant 4l mass in the 8 TeV analysis with the eventual estimation of the DPS contribution. The plot was taken from [11].

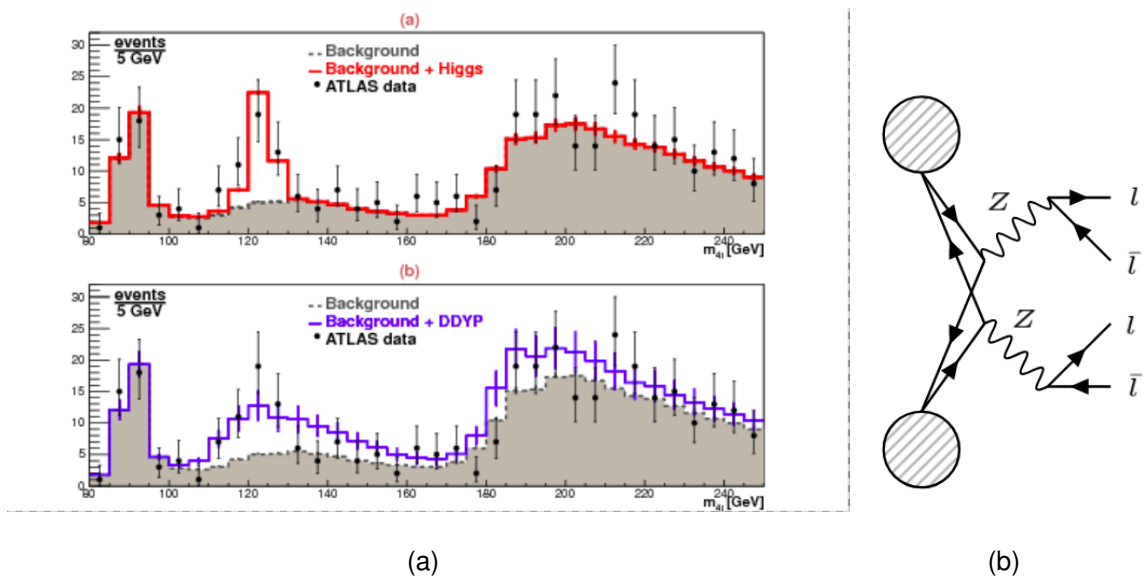


Figure 2.6: (a) The invariant mass distribution in the 4l channel in the ATLAS Higgs search analysis for the 8 TeV experiment at an early stage in 2012. The plot was taken from [13]. (b) A schematic diagram of DDY in proton-proton collisions.

Chapter 3

Experiment

The data for the analysis was collected by the ATLAS (A Toroidal LHC ApparatuS) detector in LHC. LHC is a circular particle accelerator. Currently it is the most powerful device available for hadron collisions. It accelerates bunches of about 10^{11} protons and collides them at a 13 TeV center-of-mass energy with a collision frequency of 40 GHz. It provides instantaneous luminosity of about $10^{34} \text{ cm}^{-2} \text{ s}^{-1}$. Collisions are measured in seven detectors located on the ring of the LHC, one of which is the ATLAS detector.

ATLAS is a cylindrical, general-use detector [4]. It consists of several detector system layers for detecting and characterizing passing particles. The coordinate system of ATLAS is defined with the interaction point at the origin, the z axis in the beam direction, a polar angle θ and azimuthal angle ϕ . The pseudorapidity $\eta = -\ln(\tan(\theta/2))$ is used instead of the polar angle in the analysis, because of its additive property. Transverse momentum is defined by $P_T = \sqrt{P_x^2 + P_y^2}$, where P_x , P_y are the objects momentum in the direction of the center of the LHC ring and in an upward direction respectively. The distance in the pseudorapidity-azimuthal angle space is defined by $\Delta R = \sqrt{\Delta\eta^2 + \Delta\phi^2}$.

An Inner Detector (ID) tracks particles coming from the interaction point. It is immersed in a 2T axial field. It covers $r < 1 \text{ m}$ and $|\eta| < 2.5$, where r is the radial distance from the beam. The ID consists of Pixel detectors, Silicon Micro-strip detectors and Transition Radiation Tracker. The combination of these detectors allows to reconstruct the path of charged particles.

Electromagnetic (EM) calorimeters surround the ID component and cover $|\eta| < 3.2$. In the matching η region with the ID, it has thickness of at least 22 radiation lengths.

It consists of accordion-shaped kapton electrodes in liquid-argon and lead absorption plates.

Hadronic calorimeters surround the EM calorimeters and cover $|\eta| < 4.9$. For $|\eta| < 1.7$, it consists of Tile calorimeter that has steel absorbers and scintillating tiles as active layers with minimal thickness of 9.7 interaction lengths. For $1.5 < |\eta| < 4.9$, it consists of liquid argon calorimeters with copper and tungsten absorbers.

Muon Spectrometer (MS) is surrounding the calorimeters and has a cover $|\eta| < 2.7$. It consists of Monitored Drift Tubes and Cathode Strip Chambers. It is immersed in magnetic fields with bending power between 1 to 7.5 Tm, which comes from large superconducting air-core toroid magnets. The bending power is $\int Bdl$ computed along a straight line from the interaction point.

All the detector layers have full azimuthal coverage. Electrons are absorbed in the electromagnetic calorimeter and their properties are reconstructed using the ID and EM calorimeter. Muons are usually not decaying inside the detector, and are mainly reconstructed with the deposits in the ID and MS.

The η coverage and the resolution of the various detector components of ATLAS are summarized in Table 3.1.

Table 3.1: Resolution and coverage goals of the ATLAS detector. The units for E and P_T are in GeV. Table from [20].

Detector component	Required resolution	η coverage	
		Measurement	Trigger
Tracking	$\sigma_{p_T}/p_T = 0.05\% p_T \oplus 1\%$	± 2.5	
EM calorimetry	$\sigma_E/E = 10\%/\sqrt{E} \oplus 0.7\%$	± 3.2	± 2.5
Hadronic calorimetry (jets) barrel and end-cap forward	$\sigma_E/E = 50\%/\sqrt{E} \oplus 3\%$	± 3.2	± 3.2
	$\sigma_E/E = 100\%/\sqrt{E} \oplus 10\%$	$3.1 < \eta < 4.9$	$3.1 < \eta < 4.9$
Muon spectrometer	$\sigma_{p_T}/p_T = 10\%$ at $p_T = 1$ TeV	± 2.7	± 2.4

3.1 Triggers

During the data-taking in the ATLAS, events were required to fire up triggers in order to get recorded. The triggers were also used to define an initial selection in the analysis. In this analysis triggers with signatures of a single lepton (muon or electron),

Di-lepton and Tri-lepton were used. Some of the multiple lepton triggers also allowed a combination of electron and muons. The triggers required different levels of likelihood identification, with lesser amount of leptons requiring higher level of likelihood. The triggers with their energy thresholds are summarised in Table 3.2.

Table 3.2: Summary of the P_T (E_T) trigger thresholds (in GeV) employed for the muon (electron) trigger selection in 2015, 2016, and 2017. The syntax in the table is {lepton amount}{lepton type}{threshold energy in MeV} with underscore separating trigger configurations with multiple combinations. Table from [21].

Trigger item	Trigger threshold		
	2015	2016	2017
single muon	$\mu 20$; $\mu 50$; $\mu 60$	$\mu 24$; $\mu 26$; $\mu 40$; $\mu 50$	$\mu 26$; $\mu 50$; $\mu 60$
single electron	$e 24$; $e 60$; $e 120$	$e 26$; $e 60$; $e 140$; $e 300$	$e 26$; $e 60$; $e 140$; $e 300$
dimuon	$2\mu 10$; $\mu 18_\mu 8$	$2\mu 10$; $2\mu 14$; $\mu 22_\mu 8$	$2\mu 14$; $\mu 22_\mu 8$
dielectron	$2e 12$	$2e 15$; $2e 17$	$2e 17$; $2e 24$
electron-muon	$e 24_\mu 8$	$e 24_\mu 8$; $e 26_\mu 8$ $e 17_\mu 14$; $e 7_\mu 24$; $2e 12_\mu 10$; $e 12_2\mu 10$	$e 26_\mu 8$
trimuon	$\mu 18_2\mu 4$	$\mu 11_2\mu 4$; $\mu 6_2\mu 4$; $\mu 20_2\mu 4$; $3\mu 4$ $3\mu 6$	$4\mu 4$; $\mu 20_2\mu 4$; $3\mu 4$

Chapter 4

Event Samples

4.1 Data

The analysis was performed on a set of proton-proton interactions collected during the years 2015-2017, that were recorded by the ATLAS detector at the LHC $\sqrt{s} = 13$ TeV experiment. The total of recorded integrated luminosity was 86.76 fb^{-1} . Only data that passed the standard quality requirements was used in the study, which constitutes 80 fb^{-1} .

To enable the large amount of collected data to be stored, it was required to pass some initial selection using the triggers. Every measured event was required to have at least one di-lepton and at least one fired trigger. The di-lepton was required to:

- Have invariant mass above 5 GeV.
- Have one lepton with $P_T > 15$ GeV. ("DFCommonElectronsLHLoose").
- Have a second lepton with $P_T > 5$ GeV.

4.2 Monte Carlo Samples Introduction

Monte Carlo (MC) simulation of the detector and the measured processes is important for any experiment in high energy physics for several reasons:

- Acceptance: Some parts of each event are always left unmeasured due to inability to cover up the whole phase space. That includes, for example, particles

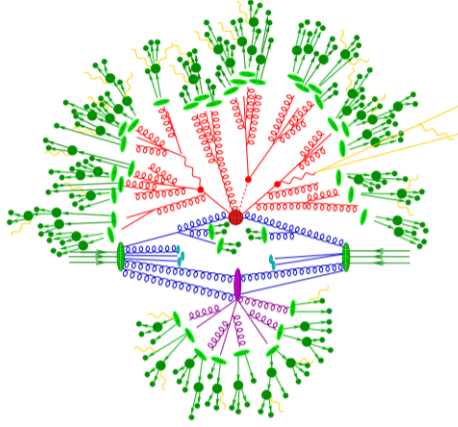


Figure 4.1: Pictorial representation of a $t\bar{t}H$ event as produced by an event generator. The hard interaction (big red blob) is followed by the decay of both top quarks and the Higgs boson (small red blobs). Additional hard QCD radiation is produced (red) and a secondary interaction takes place (purple blob) before the final-state partons hadronise (light green blobs) and hadrons decay (dark green blobs). Photon radiation occurs at any stage (yellow). Plot was taken from [22].

that are not interacting with the detector and angles in which the detector has no coverage. The simulation allows to complete the missing information.

- Resolution: All the measuring devices in the detector have some measuring uncertainty. The simulation of the measuring device allows to estimate it.
- Reconstruction Efficiency: the simulation of the detector also allows to estimate the amount of True Negative (TN) and False Positive (FP) measurements. It is usually important because the amount of TN particles is much higher than FP particles. That happens because the density in the limits of the detectors phase space is steep and the amount of particles that are getting measured due to uncertainty is bigger than the amount of particles that are missed.

A schematic representation of a diagram of the whole generation process is showed in Figure 4.1. The possible initial particles (blue) are given by the PDF. The hard process (red) is calculated using the SM matrix element calculations. The evolution of the initial (blue) states or final state of the hard interaction (red) is called the parton shower. The transition from the final states in the parton shower to colorless hadrons is called hadronization (light green blobs). Afterwards there is the hadron decay (dark

green) into particles that pass through the detector. Some calculations in the generation, like the choice of PDF and the hadronization processes, are phenomenological, in the sense that there are parameters in the process that can be varied. The choice of these parameter values is called tuning. For analyses in ATLAS, each part of each process generation is frequently simulated with different programs and tuning in order to get a simulation that best fits the observations.

4.3 Produced MC Samples

The MC samples for this analysis were produced mostly using Powheg [23]. In Powheg generated samples, CT10 PDF [17] was used for the hard process. For the parton shower and hadron decay Powheg was interfaced with Pythia8 [24] and either CTEQL1 [25] or NNPDF23LO [26] PDFs were used. Non-perturbative effects were simulated with AZNLO [27] or A14 tunes. In the A14 tune the initial and the final state radiation parameters are set to fit ATLAS data, that was collected at $\sqrt{s} = 7$ TeV [28]. For the hadron decay Powheg was also interfaced with EvtGen [29] to simulate the B and C hadron decays. For loop induced diboson production ($gg \rightarrow ZZ$) the generation was done with gg2VV [30]. Two top quarks with a Z boson production (ttZ) was generated using MadGraph (NLO) [31]. Some of the samples were generated with Sherpa [22] using NNPDF30 PDF set [18].

Additionally to the standard MC samples, that were retrieved from the group conducting Higgs decay into two $Z^{(*)}$ bosons (the HZZ group), a DY simulation with only 2 measured leptons in the final state was used. There were several simulation samples of DY in different mass range in order to get sufficient statistics in higher mass regions.

After the generation, the particles passage through the ATLAS detector was simulated [32], in order to translate the generated particles to the reconstructed particles that were measured in the detector.

All the samples produced were for SPS processes only. The simulation of DPS processes, which are DDY processes in the four lepton channel, was done by overlaying the analysed events from the DY simulation later in the analysis.

The samples in the analysis were categorized as:

- SPS-signal for all SPS processes with four leptons coming from the decay of

$Z^{(*)}Z^{(*)}$ that can potentially be DDY (fully leptonic diboson processes with Z bosons). Consists of: $Z^{(*)}Z^{(*)}$ production from quark-antiquark ($q\bar{q}$) and quark-gluon (qg) initial states; EW correction for $Z^{(*)}Z^{(*)}$ production with additional partons in the final state; loop induced diboson production from gluon-gluon (gg) initial state; Higgs production in gluon fusion (ggF), vector boson fusion (VBF), associated production with a vector boson (VH), associated production with a single top (tH) and associated production with $t\bar{t}$ ($t\bar{t}H$).

- SPS-background for all SPS processes with four leptons in the final state that don't originate from the decay of prompt $Z^{(*)}Z^{(*)}$ and can't be potentially misidentified with DDY. Consists of: Triboson production (VVV) that includes Higgs associated production with $Z^{(*)}$ boson where the Higgs decays into two charged leptons; single boson with additional jets processes ($Z + jets$); diboson production processes, where one of the bosons is W instead of Z (WZ); two top quarks with a Z boson production ($t\bar{t}Z$); two top quarks production ($t\bar{t}$), where the top quarks only decay leptonically;
- DPS for the DDY samples. This sample was artificially produced by pairing events from DY samples.

The MC samples were required to pass the same initial selection that was done on the data. In order to have a simulation of DPS, randomly chosen DY event pairs were overlayed. The DY events were taken from a simulation and not from the data, because there was no available data sample whose lepton selection was with low enough energy trigger for the purposes of the analysis. The additional lepton pair in the study can have a mass as low as 12 GeV. To ensure the availability of such pairs in the simulation, the initial selection was applied for the overlayed DY events but not for the DY. This way it was guaranteed that the distribution of the generated leptons in the DPS sample will be similar to the one in the SPS sample. Table 4.1 sums up the simulation samples.

Table 4.1: Simulation samples in the analysis and their properties. For the Powheg generator different PDF sets are used for the hard process and the parton shower.

The VVV process includes ZH where H decays into two charged leptons.

Category	Process	Generator	PDF	Tune	k-factor
SPS-signal	$qq/qg \rightarrow ZZ$	Powheg	CT10+CTEQL1	AZNLO	m_{4l} dependent [33, 34]
	$H(ggF, VBF, VH, tH)$	Powheg	CT10+CTEQL1	AZNLO	
	$H(ttH)$	Powheg	CT10+NNPDF23	A14	
	$qq \rightarrow ZZ$ EW corrections	Sherpa	NNPDF30NNLO		
	$gg \rightarrow ZZ$	gg2vv	CT10+NNPDF23	A14	1.7 [35]
SPS-background	VVV	Sherpa	NNPDF30NNLO		
	$Z + jets$	Sherpa	NNPDF30NNLO		0.9751
	WZ	Powheg	CT10+CTEQL1	AZNLO	
	$t\bar{t}Z$	Madgraph	CT10+NNPDF23	A14	1.1949
	$t\bar{t}$	Powheg	CT10+NNPDF23	A14	1.1398
DPS	DY for DDY	Powheg	NNPDF30NLO		

Chapter 5

Selection

For this study all the MC samples were analysed using a software provided by the HZZ group. Their selection was tuned for researching the Higgs particle and its decay via $Z^{(*)}$ bosons to four leptons. All the samples, aside from to the DY, were initially pre-selected in the same way as the data, requiring for each event the existence of at least one energetic di-lepton. The DY processes were not required to pass the pre-selection because otherwise the resulting DPS has a different phase space from the SPS samples and the data.

5.1 Selection

The selection in the analysis presented here follows the selection of Higgs measurements in the four lepton channel [36, 21]. That included the choice of triggers, identification and reconstruction of the particles in the detector and the pairing conditions. Electrons were identified from matching reconstructed tracks in the ID and energy deposits in the EM calorimeter. To minimize the background on the detected electrons, they were required to have $E_T > 7\text{GeV}$, $|\eta| < 2.47$, and pass a likelihood discrimination. Muons had several algorithms of identification and reconstruction that use information from separate parts of the detectors [37]:

- Standalone (SA) and Silicon-associated forward (SiAF): Using only MS and Calorimeter energy deposits. Muon segments were found in the MS, extrapolated to the interaction point and then refitted, taking into account the energy loss in the calorimeters. The resulting track is called muon extrapolation (ME). These types

of muons were employed only for $2.5 < |\eta| < 2.7$, where the ID has poor coverage.

- Combined (CB): Using the ID, Calorimeters and MS. This algorithm pairs the ME tracks with ID tracks, then does a combined fit. These type of muons were employed for $0.1 < |\eta| < 2.5$.
- Calorimeter tagged (CT) : Using a track in the ID and energy deposits in the Calorimeters (without information from MS). These types of muons were employed only for $|\eta| < 0.1$, which was not covered by the MS.
- Segment tagged (ST): Using ID and MS. Employed only for $|\eta| < 0.1$, too.

The CT muons detection was optimized for $P_T > 15$ GeV, all other muons had $P_T > 5$ GeV. With the reconstruction algorithms combined, the detected muons were measured for $|\eta| < 2.7$. To reduce measurements of cosmic muons, the measured muons were required to have $d_0 < 1$ mm, where d_0 is the transverse impact parameter with respect to the beam-line. The primary vertex, in a given bunch collision, was selected to be the one with the largest sum on emerging tracks P_T . Lepton tracks were required to have $|z_0 \sin \theta| < 0.5$ mm, where z_0 is the track distance from the vertex along the beam-line and θ is the polar angle of the track, to ensure they were originating in the primary vertex. The selection for individual leptons is summarized in Table 5.1.

Table 5.1: Selection of individual leptons

	Electrons	Muons
E_T/P_T	> 7 GeV	> 5 GeV (15 GeV for CT muons)
$ \eta $	< 2.47	< 2.7
$Z_0 \sin \theta$	< 0.5 mm	< 0.5 mm
d_0	< 1 mm	< 1 mm (aside from SA muons that have no track)

Further selection takes into account that the signal is a process of two Z bosons production and their leptonic decay. An event was required to include at least four leptons in the final state. The leptons were paired into di-leptons for all possible Same-Flavor-Opposite-Charge (SFOC) combinations. The di-leptons were paired into quadruplets so that in each quadruplet:

- The same lepton could not contribute to a quadruplet more than once;
- No more than one muon of the CT, SA or SiAF types was allowed;
- The P_T thresholds for the three leading leptons, after ordering them by P_T , were 20, 15 and 10 GeV;
- The di-lepton with the invariant mass closest to the Z mass value, as published by the Particle Data Group [38], was defined as the "leading" and the other one as the "sub-leading";
- The leading di-lepton mass was required to be between 50 and 120 : GeV;
- The sub-leading di-lepton mass was required to be below 120 GeV and above a threshold that was 12 GeV for $m_{4l} \leq 140$ GeV, was increased linearly to 50 GeV for $m_{4l} \in [140 \text{ GeV}, 190 \text{ GeV}]$, and stayed fixed at 50 GeV for $m_{4l} \geq 190$ GeV;

The cuts for the quadruplets maximized the signal in the Higgs search analysis. It was essential to use them in this study to ensure that the simulation describes the data. To minimize contributions from low mass J/ψ resonance and some other backgrounds, additional isolation requirements were applied on each quadruplet. Any two SF(Opposite-Flavor, OF) leptons had to have $\Delta R > 0.1(0.2)$. Alternative SFOC di-leptons were required to have invariant mass above 5 GeV. Isolation cuts were applied for the leptons, where muons were required to have $P_T^{\text{varcone}30}/P_T < 0.15$ and $E_T^{\text{topocone}20}/P_T < 0.3$, and electrons were required to have $E_T^{\text{varcone}20}/E_T < 0.15$ and $E_T^{\text{topocone}20}/E_T < 0.2$. Here the numerator is the sum on the surrounding objects without the other leptons in the quadruplet; "varcone" means taking track measurements in the ID and "topocone" means taking the measurements in the calorimeters, and the value after is the $\Delta R * 10$ of the considered cone; The denominator is the E_T or P_T value for the relevant lepton. The d_0 significance was required to be less than 5 for electrons and less than 3 for muons. $\chi^2/NDOF$ of the vertex fit was required to be less than 6 for four muons quadruplet and less than 9 for any other combination. The selection of quadruplets is summed up in table 5.2.

Table 5.2: Methodology of quadruplets formation and consequential requirements in each event

Short name	description
Leptons	At least 4 lepton.
SFOC	lepton pairing: each pair had to form same-flavor opposite charge leptons di-lepton pairing (making quadruplets): no overlapping leptons in the pairs Leading pair is the one with invariant mass closer to PDG Z mass No more than one CT, SA or SiAF muon in a quad
Kinematic	At least one lepton with $P_T > 20$ GeV, two with $P_T > 15$ GeV, three with $P_T > 10$ GeV
Z1 mass	Leading Z mass has to be between 50 and 120 GeV
Z2 mass	sub-leading Z mass has to be between 12 and 120 GeV, with a stricter lower threshold for m_{4l} above 140 GeV
DeltaR	For any combination of two leptons in the quad $\Delta R > 0.1$ if SF, $\Delta R > 0.2$ if Opposite Flavoured(OF)
Jpsi	Quadruplets are rejected if any two SFOC leptons has invariant mass under 5 GeV
Isolation	$P_T^{varcone30}/P_T < 0.15$ and $E_T^{topocone20}/P_T < 0.3$ for muons $E_T^{varcone20}/E_T < 0.15$ and $E_T^{topocone20}/E_T < 0.2$ for electrons
d_0 significance	< 5 for electrons, < 3 for muons
vetex quality	$\chi^2/NDOF < 6$ for four muons, < 9 for the rest

5.2 DPS Construction

The DY was required to pass similar selection without the cuts related to 4 leptons or high energies, which includes: the initial selection, a cut on lepton amount, quadruplet amounts cut, kinematic cuts and Z masses restrictions. Figure 5.1 shows the distribution of the DY invariant mass after the selection. The combination of DY events into

DDY was executed according to the following rules:

- Each DY event was used no more than once in the combinations.
- Only DY events with a single SFOC possible di-lepton configuration were used for the combinations.
- A combination was required to have a distance of less than 1 cm between reconstructed DY vertices.
- At least one of the combined di-leptons had to have an invariant mass higher than 10 GeV and a lepton with P_T above 15 GeV to simulate the effect of the initial selection.

A total of 100k DPS events were constructed. The constructed DPS then passed a similar selection as data and SPS. Differently to SPS, the isolation cuts that required the "topocone" and "varcone" measurement were not performed, and DPS events with more than 4 leptons were filtered. The selection had about 60% efficiency on the generated DPS events. The efficiency decrease comes mostly from the Z mass requirements that were not accounted for in the construction process.

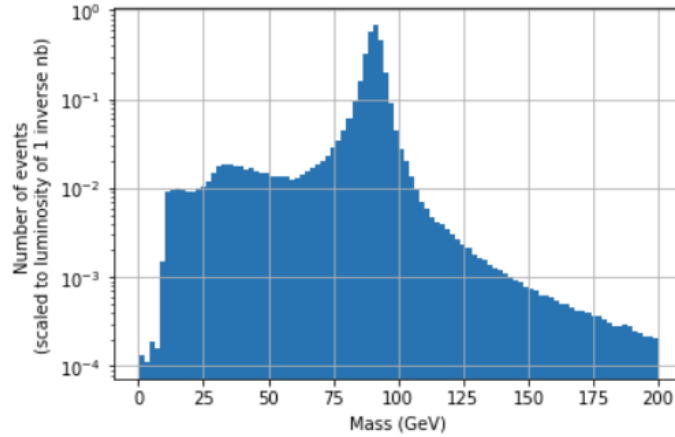


Figure 5.1: The distribution of the invariant mass of the simulated DY events that passed the selection. All the DY MC samples were re-weighted to the same luminosity.

Chapter 6

Background and Uncertainties

6.1 Correction to MC

In order to get a good reproduction of the data by MC, some correction had to be applied to the simulated samples. Some of the corrections were included as multiplicative weights in the resulting files retrieved from the HZZ groups software. The simulated data in the analysis contained the following weights for each events:

- Theoretical cross section (k factors included) - The theoretical probabilities of the simulated process.
- Branching ratio (for Higgs simulation where only lepton decays were simulated)
 - For the Higgs sample only fully leptonic decays were simulated and therefore the cross section of the Higgs productions had to be multiplied by the branching ratio of these decays.
- Luminosity factor - the integrated luminosity of the measurements the MC sample was simulated for. Separate samples were simulated for 2015-2016,2017 and 2018.
- B tag and lepton efficiencies
- Trigger scale factors - the ratio between tagging efficiencies in data and MC.
- EW corrections - correction to the cross sections that originate from taking into account electro-weak interactions.

- MC weights - theoretical corrections that has to be applied to the MC due to its production way.
- Pileup - scaling of the number of simulated proton-proton collusion for a single proton bunch crossover to the number measured in the data.

6.2 Estimation of Misidentified and Prompt Leptons

As described in Chapter 4, the SPS-background are processes with four leptons in the final state that can't be misidentified with DDY, and the SPS-signal are processes that can be misidentified with DDY. The SPS-background consists of $Z + Jets$, $t\bar{t}$ and WZ processes, with misidentified electrons or prompt muons creating a topology similar to the signal. Additionally, the SPS-background includes the VVV and $t\bar{t}V$ processes which can have four correctly identified leptons that are not originating from two $Z^{(*)}$ boson decays. The cross section of processes with wrongly measured leptons can not be estimated by MC.

The general method for estimating the yield of a background that can not be simulated by MC is:

- Collect and simulate data in a Control Region (CR), which is a phase-space measured by the detector, that is enriched with the background events and is also orthogonal to the Signal Region (SR), where the signal process is measured.
- Fit the MC to the data in the CR to estimate the normalization correction that needs to be applied to the simulated background.
- Translated the resulting normalization values to the SR using transfer factors that are also estimated from simulation.

The above method was used to determine the normalization of $Z + jets$ and $t\bar{t}$ processes. Different CRs were used for $ll + \mu\mu$ and $ll + ee$ final states, because background muons mostly originate in heavy flavor decay, and background electrons mostly originate in misidentified light flavor jets.

The normalization of $ll + \mu\mu$ final states was estimated using a two-step fit of the invariant leading lepton pair mass in several CRs:

- inverted d_0 CR: The vertex quality cut was not applied and the d_0 cut on the sub-leading lepton pair was inverted.
- $e\mu + \mu\mu$ CR: The vertex quality cut was not applied, the leading pair was required to be with different-flavour leptons, the sub-leading pair had no requirements on d_0 and isolation, pairs of same-charged and opposite-charged muons were both accepted for the sub-leading pair.
- inverted isolation CR: The sub-leading lepton pair was required to have at least one lepton that didn't pass the isolation cut.

The $Z + jets$ sample was divided into heavy and light flavoured jets ($Z + HF$, $Z + LF$). The normalization of $Z + HF$ and $t\bar{t}$ was estimated from simultaneously fitting the MC contribution in the inverted d_0 CR and in the $e\mu + \mu\mu$ CR to the data. Afterwards, the normalization of the $Z + LF$ contribution was determined from fitting MC to the data in the inverted isolation CR, after fixing the normalization of the other components.

The yield of processes with $ll + ee$ final states was estimated in a $3l + X$ CR: The selection and identification requirements on the lowest P_T electron in the sub-leading pair consisted of having a number of hits in the ID and of passing the d_0 cut. Additionally, only same-charged electrons were accepted in the sub-leading pair.

The uncertainties for the background estimation originated both from the fit in the CRs and from the transfer factors.

The implementation of this part of the analysis was beyond the scope of this study. In order to get an estimate of the normalization and of the systematic uncertainty imposed from the described process, the results of the HZZ group in [21] were compared to the results of the available MC. The samples of $t\bar{t}$ and $Z + jets$ were normalized to the expectation of the HZZ group. The systematic uncertainty was associated to the $Z + jets$ process, because it had bigger influence on the results. The extracted numbers are presented in Table 6.1.

Table 6.1: The number of MC events with four lepton invariant mass above 130 GeV, according to the results of [21]. compared to the available simulation. For the full invariant mass range the results presented in [21] were scaled.

Range	From selected simulation	From external study
Above 130 GeV	31.4	47.5 ± 9.3
Full range (extrapolated for the external study)	42	64 ± 14

6.3 Overall Scale

There was a known issue of approximately 10% bias between the data and MC in the experiment in the expected number of events. The method of signal extraction used in this study depends only on the shape of the SPS-signal. Therefore, an overall bias can only affect the DPS estimation result via the scaling of the SPS-background samples. For events with invariant mass between 300 and 500 GeV, it was assumed that the amount of DPS is negligible. The difference between data and MC in this range was 12.67%. All the SPS MC samples were scaled by this amount, and the difference in normalization of each process was added to its systematic uncertainty.

6.4 Uncertainties

The uncertainties of the MC were calculated in the following way:

- Statistical uncertainty.
- The $Z + jets$ MC sample systematic uncertainty includes the background estimation with $t\bar{t}$.
- The samples of the $gg \rightarrow ZZ$ process were estimated to have a 60% relative uncertainty due the big theoretical uncertainties of the k-factor [39].
- All the MC processes have additional relative systematic uncertainty of 12.67% from the overall scaling.

The expected number of MC events used in the analysis after all the correction were applied is presented in table 6.2.

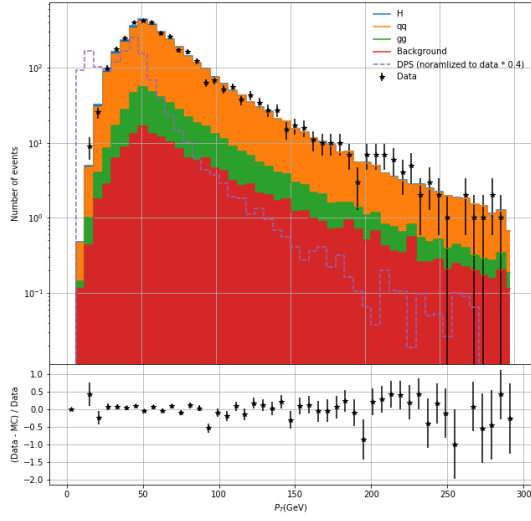
Table 6.2: The expected amount of events in each MC process. The first and second quoted uncertainties correspond to the statistical and systematic uncertainties, respectively. For the total MC and for the data, only the statistical uncertainty is quoted.

Process	Expected number of events
gg	$312.52 \pm 0.68 \pm 227.11$
$q\bar{q}$	$2673.7 \pm 9.1 \pm 338.8$
$q\bar{q} + jj$	$30.7 \pm 0.12 \pm 3.89$
H	$136.33 \pm 0.17 \pm 17.27$
VVV	$17.135 \pm 0.065 \pm 2.171$
WZ	$10.08 \pm 0.44 \pm 1.28$
$Z + Jets$	$42.2 \pm 1.0 \pm 19.3$
$t\bar{t}$	$27.3 \pm 2.5 \pm 3.5$
$t\bar{t}V$	$54.78 \pm 0.27 \pm 6.94$
Total MC	3305 ± 10
Data	3363 ± 58

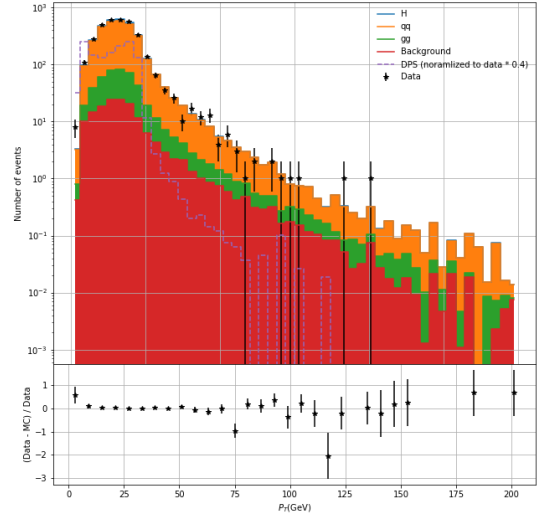
The systematic uncertainties of the final result originating from the detector calibration uncertainties were also calculated in the course of this study. However, due to a bias they were not included in the uncertainty estimates of the final result. The effect of detector calibration on the final result was assumed negligible based on the previous measurement of DPS in the 8 TeV experiment [11]. This part of the study is explained in appendix B.

6.5 Control Plots

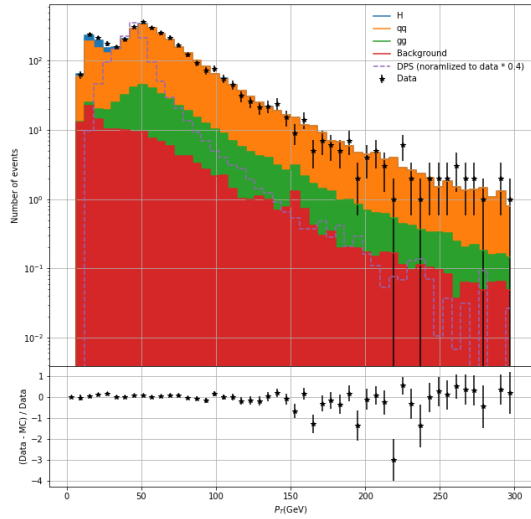
The distributions of different variables for the data, SPS and DPS after the selection are given in Figures 6.1, 6.2, 6.3, 6.4, 6.5 and 6.6. The control plots show that there is a good agreement between the data and the simulation. For the four lepton invariant mass it can be seen that the DPS distribution is similar to the ones obtained in [12],[13], with peaks in the vicinity of the Higgs and the two Z bosons masses.



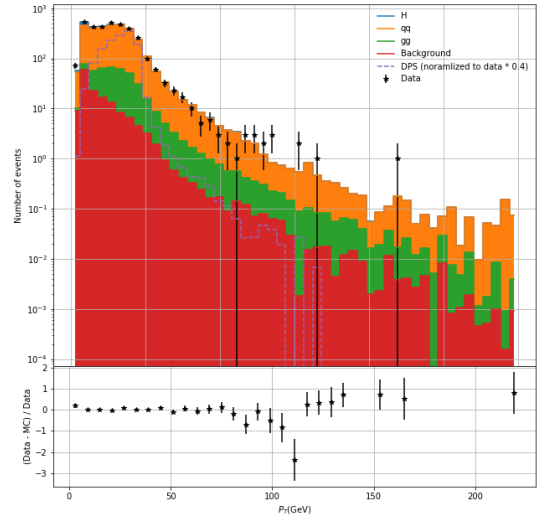
(a) Higher P_T lepton from the leading pair



(b) Lower P_T lepton from the leading pair

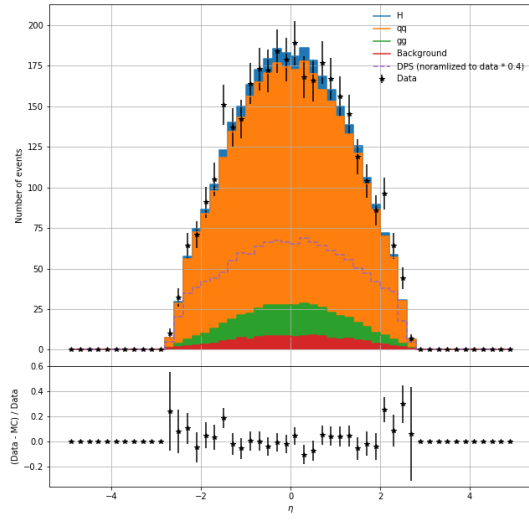


(c) Higher P_T lepton from the sub-leading pair

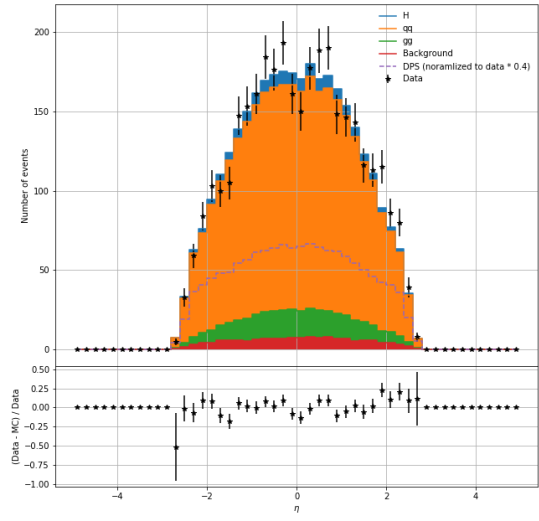


(d) Lower P_T lepton from the sub-leading pair

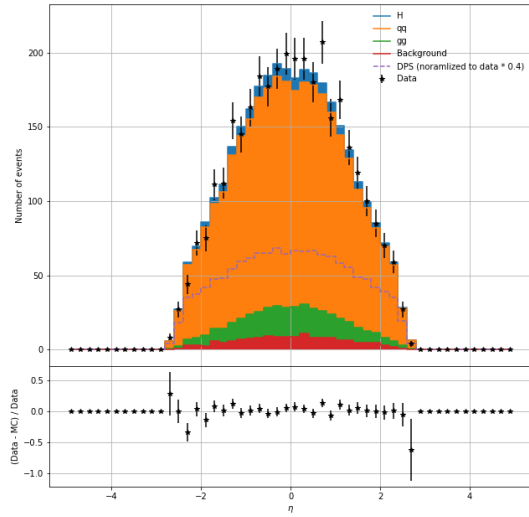
Figure 6.1: Distributions of the P_T of individual leptons selected in the study. Comparison of the data distributions to staggered MC. The SPS samples are staggered. The DPS sample was scaled to 40% of the data. In addition, a ratio plot between data and sum of the SPS samples is presented in each graph, showing the agreement between the data and the simulation.



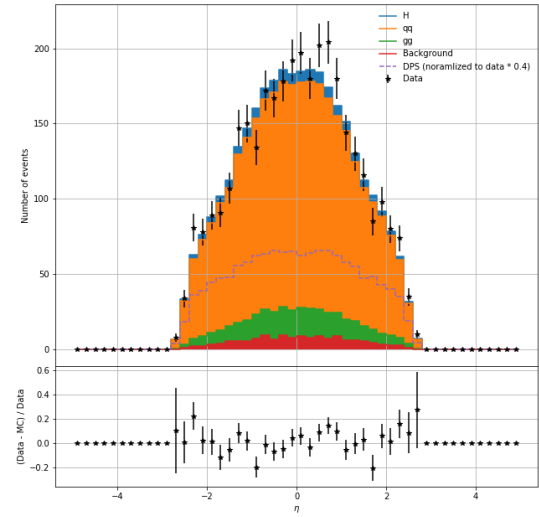
(a) Higher P_T lepton from the leading pair



(b) Lower P_T lepton from the leading pair

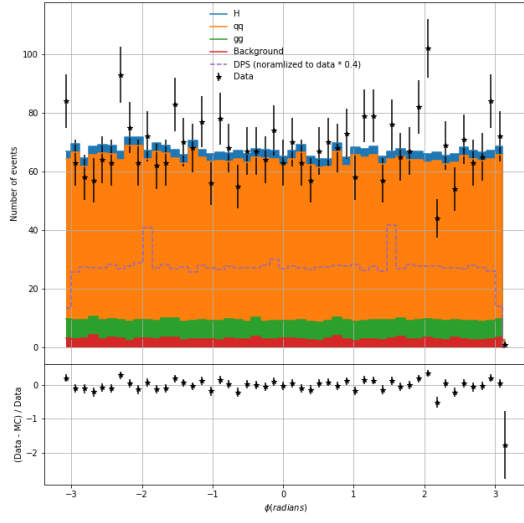


(c) Higher P_T lepton from the sub-leading pair

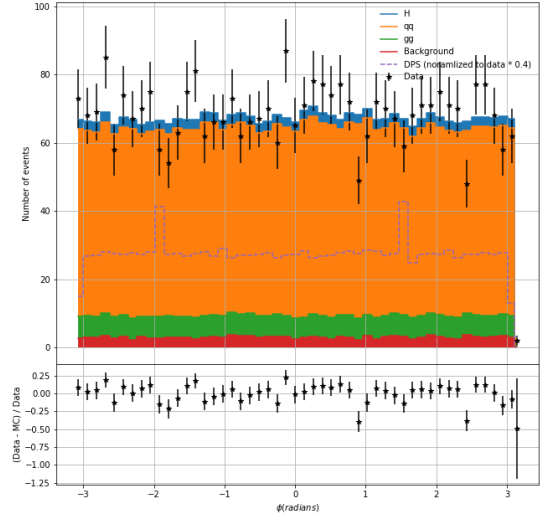


(d) Lower P_T lepton from the sub-leading pair

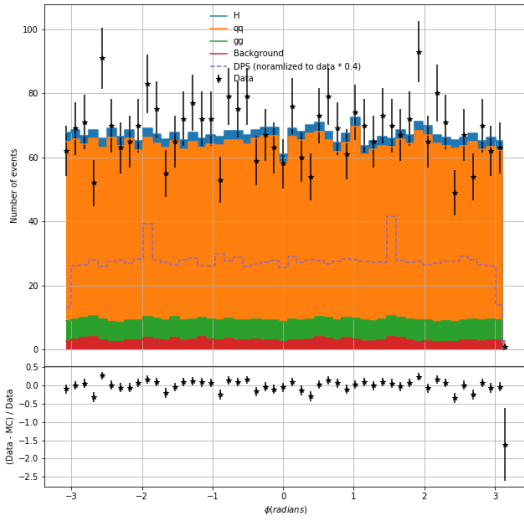
Figure 6.2: η distribution of individual leptons. The rest as described in Figure 6.1



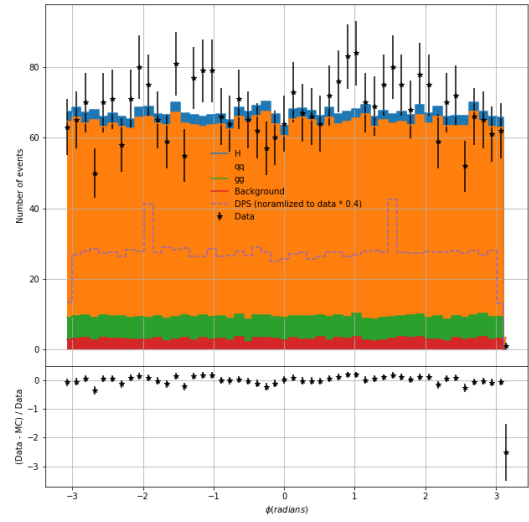
(a) Higher P_T lepton from the leading pair



(b) Lower P_T lepton from the leading pair

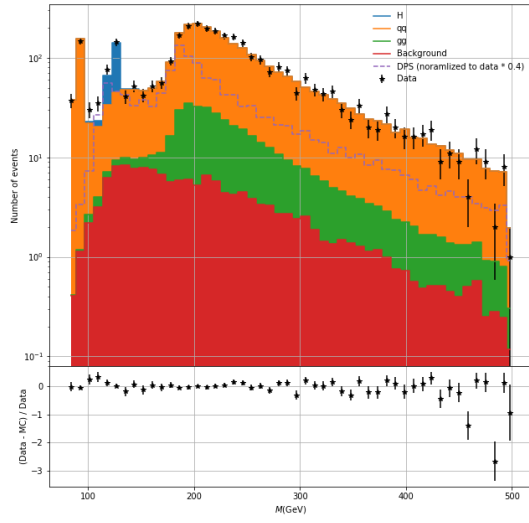


(c) Higher P_T lepton from the sub-leading pair

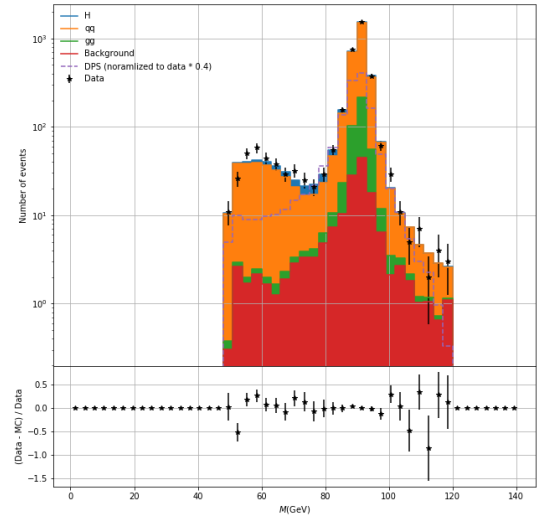


(d) Lower P_T lepton from the sub-leading pair

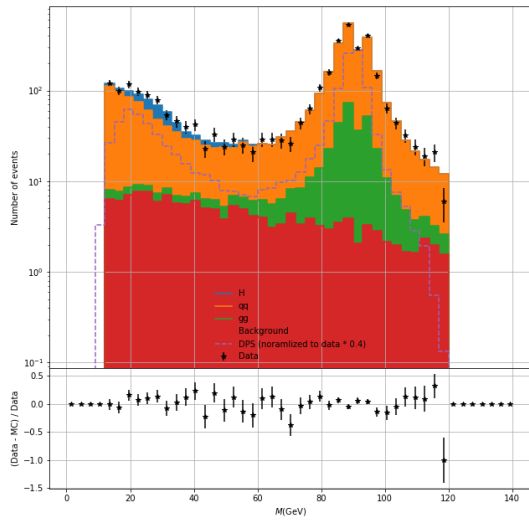
Figure 6.3: ϕ distribution of individual leptons. The rest as described in Figure 6.1.



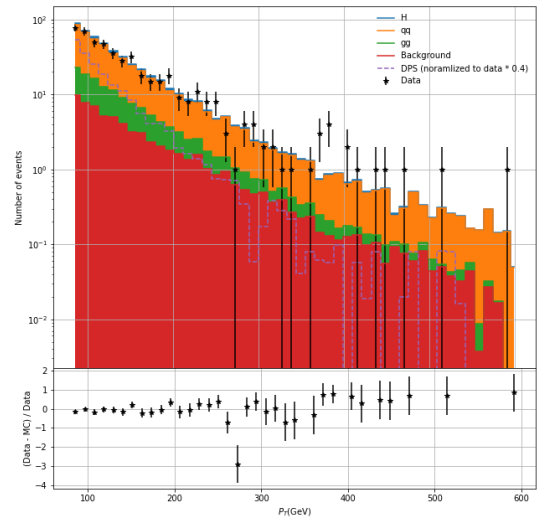
(a) Four lepton invariant mass



(b) Leading di-lepton invariant mass

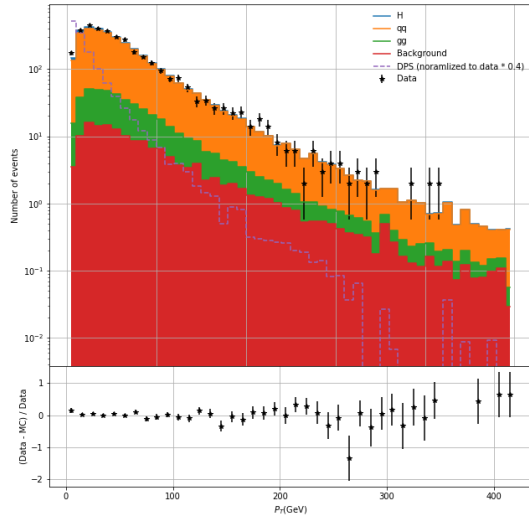


(c) Sub-leading di-lepton invariant mass

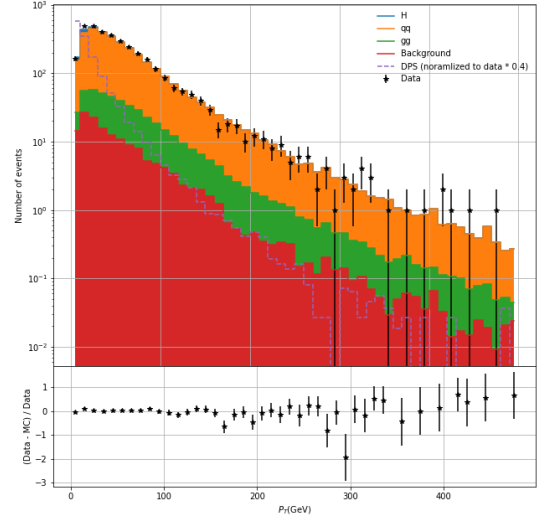


(d) Four lepton P_T

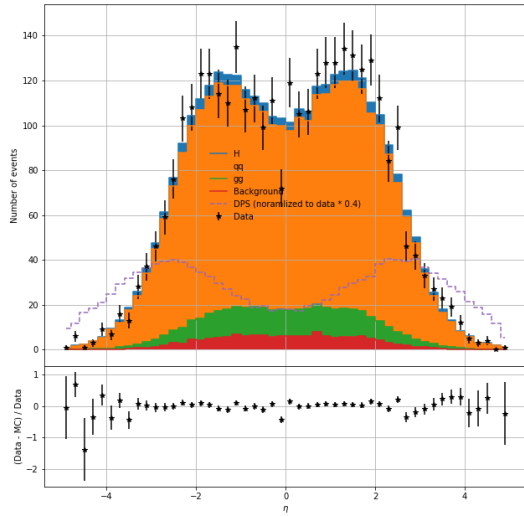
Figure 6.4: P_t and invariant mass distributions of lepton combinations. The rest as described in Figure 6.1.



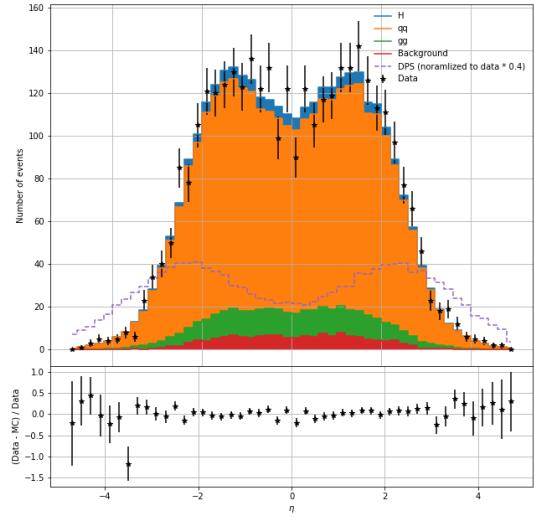
(a) Leading di-lepton P_T



(b) Sub-leading di-lepton P_T

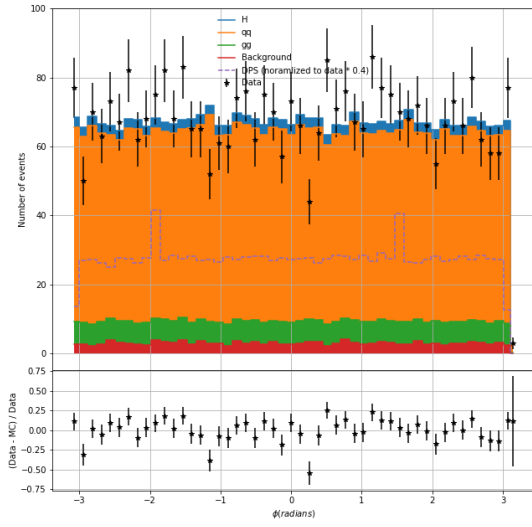


(c) $\Delta\eta$ between the leading di-leptons leptons

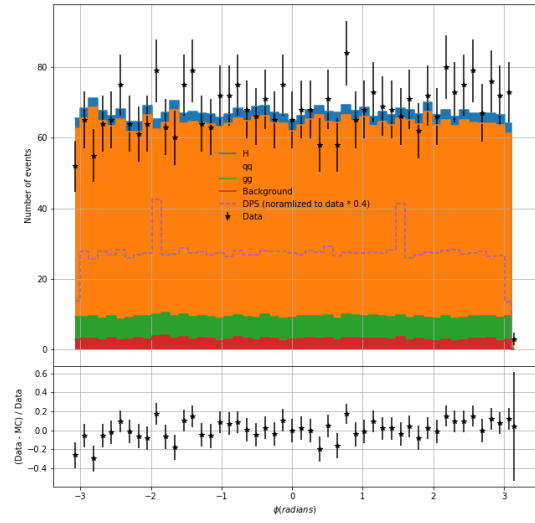


(d) $\Delta\eta$ between the sub-leading di-leptons leptons

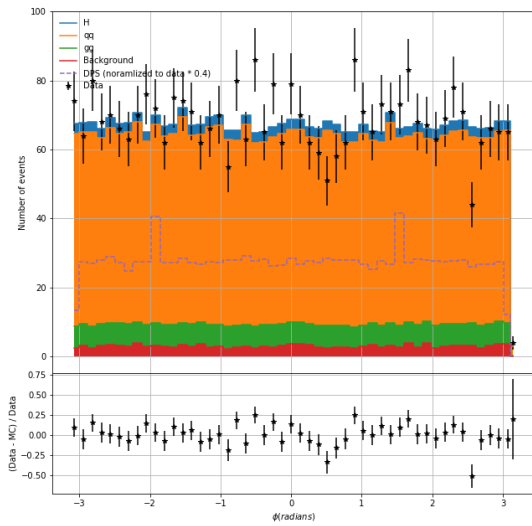
Figure 6.5: P_t and η distributions of the dileptons. The rest as described in Figure 6.1.



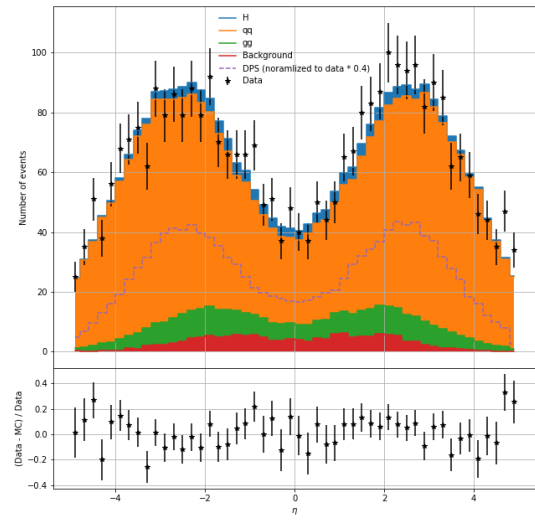
(a) $\Delta\phi$ between the Z bosons



(b) $\Delta\phi$ between the leading di-leptons leptons



(c) $\Delta\phi$ between the sub-leading di-leptons leptons



(d) $\Delta\eta$ between the Z bosons

Figure 6.6: ϕ and η differences between the leptons and the Z bosons. The rest as described in Figure 6.1.

Chapter 7

Methodology of DPS Fraction Extraction

7.1 Discriminating Variables

The distinction between DPS and SPS events was done using 21 discriminating variables. The choice of variables was the same as in earlier studies of DPS in four-jet and four-lepton channels [40, 11]. The variables included:

- Transverse momentum balance : $\Delta_{ij}^{P_T} = \frac{|\vec{P}_T^i + \vec{P}_T^j|}{|\vec{P}_T^i| + |\vec{P}_T^j|}$
- Azimutal angle between leptons : $\Delta\phi_{ij} = |\phi_i - \phi_j|$
- Rapidity difference between leptons : $\Delta y_{ij} = |y_i - y_j|$
- Azimutal angle between di-leptons : $\Delta\phi_{ijkl} = |\phi_{i+j} - \phi_{k+l}|$

Here i, j, k, l are the indices of the lepton in a chosen quad ordered by the leading and sub-leading pair and then by the lepton P_T . ϕ_{i+j} is the azimuthal angle of the vectorial sum of lepton's i and j tracks. The variables were selected under the assumption that the Z bosons in a DPS event are not correlated, which leads to a different relative spacial behavior of the final state objects as compared to SPS. The intuition behind that is that the di-leptons in DPS processes has zero P_T in reference to the interaction point and would scatter back-to-back. In SPS processes the di-leptons have high P_T which can result in the di-leptons scattering in random directions. The topology is

graphically presented in Figure 7.1. The distribution of each discriminating variable in SPS, DPS and the data is shown in Figures 7.2, 7.3, 7.4 and 7.5. It is consistent with the intuition that the best variables to discriminate between DPS and SPS are:

- $\Delta\phi_{1234}$ in Figure 7.2
- $\Delta\phi_{12}$ and $\Delta\phi_{34}$ in Figure 7.3
- ΔP_{12}^{PT} and ΔP_{34}^{PT} in Figure 7.4

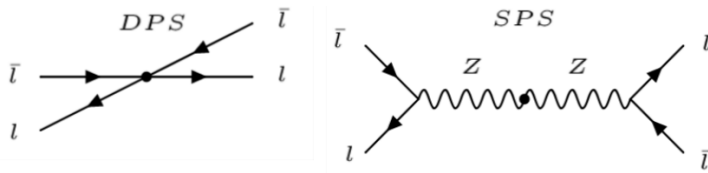
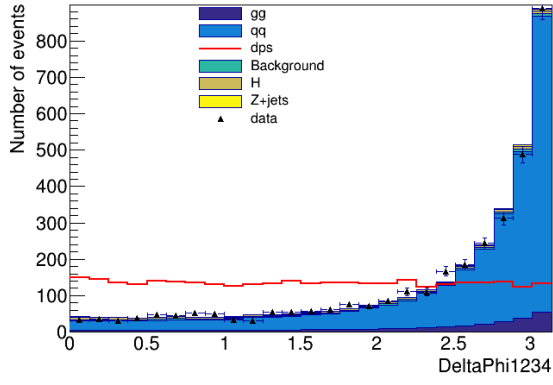
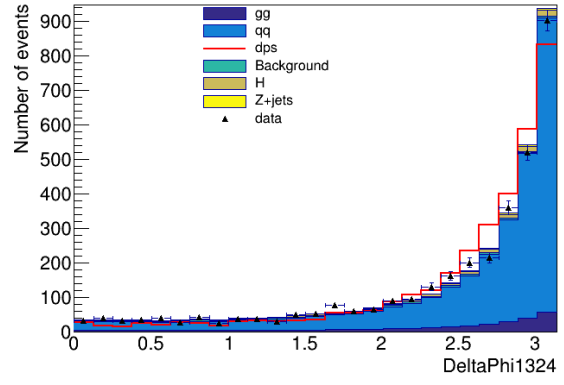


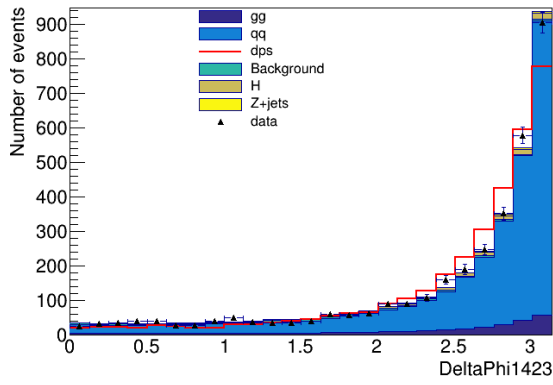
Figure 7.1: Graphic representation of the scattering topology of the DPS and SPS-signal processes. The black dot is the interaction point, for which the event has small transverse momentum in the laboratory's frame of reference. The Z^* bosons in the DPS are decaying in the interaction point, while for the SPS processes they can be on-shell and therefore long living.



(a) DeltaPhi1234

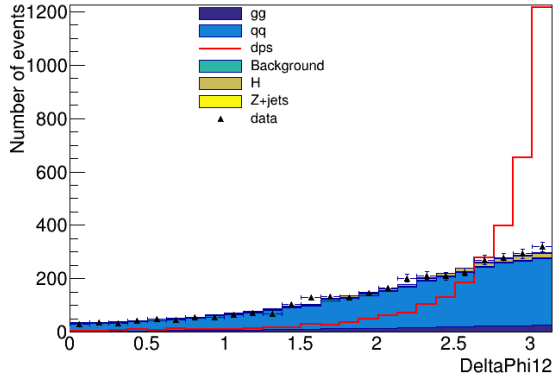


(b) DeltaPhi1324

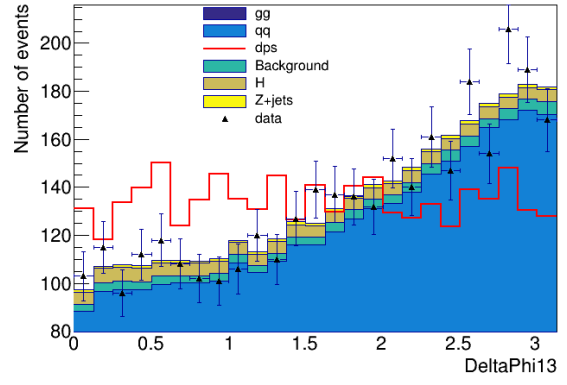


(c) DeltaPhi1423

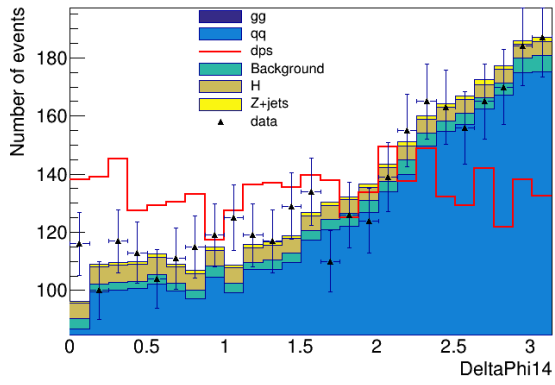
Figure 7.2: Distributions of the azimuthal angle between the di-leptons constructed in all possible ways without demanding SFOC



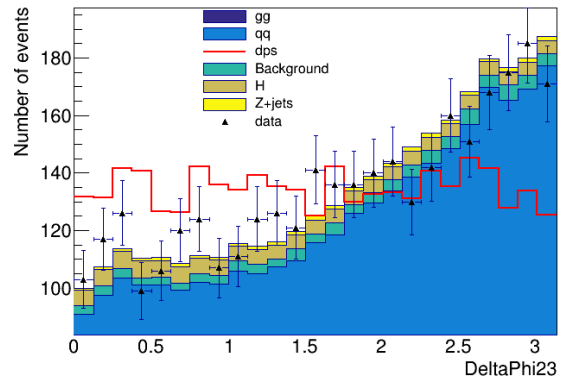
(a) DeltaPhi12



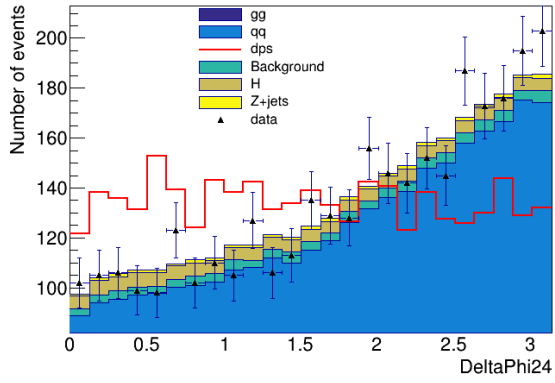
(b) DeltaPhi13



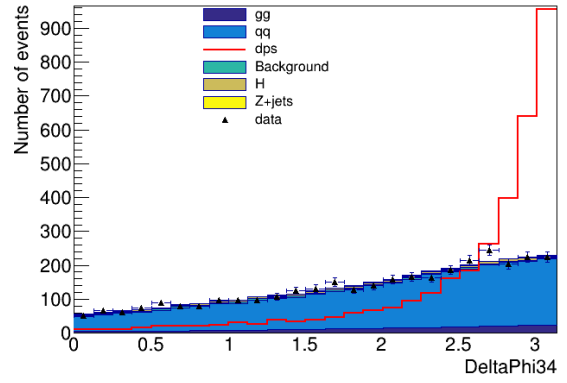
(c) DeltaPhi14



(d) DeltaPhi23

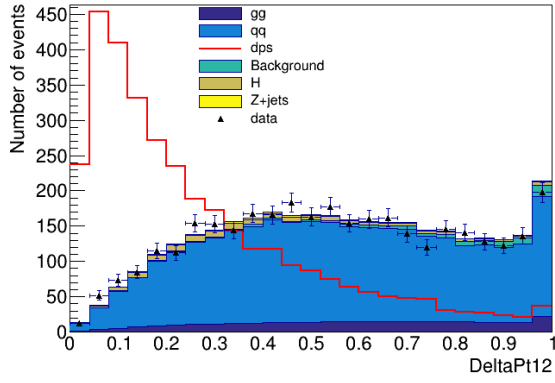


(e) DeltaPhi24

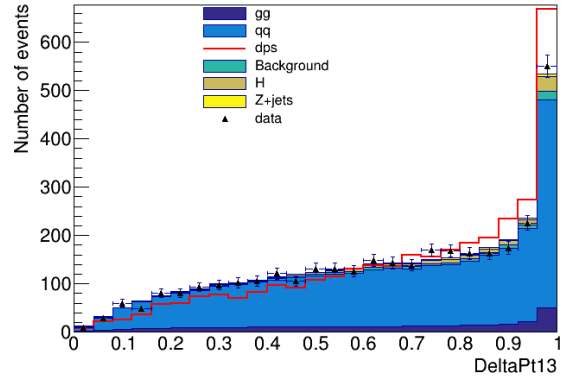


(f) DeltaPhi34

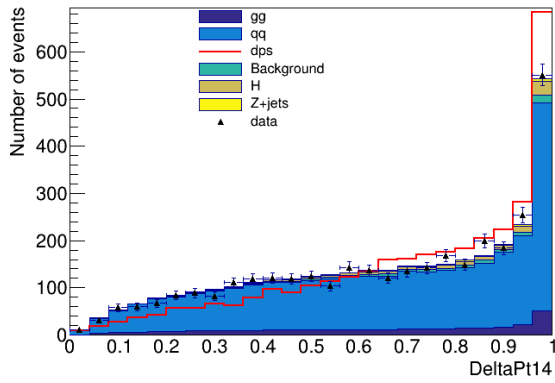
Figure 7.3: Distributions of the azimuthal angle between any two leptons



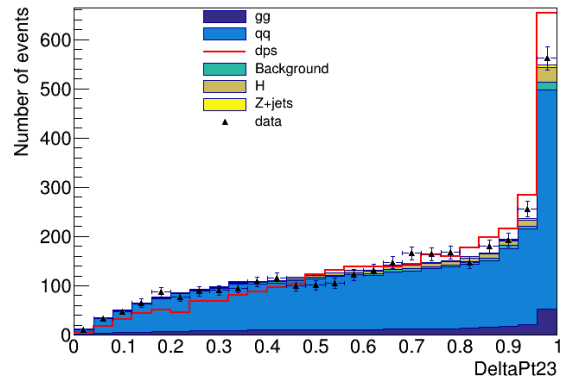
(a) DeltaPt12



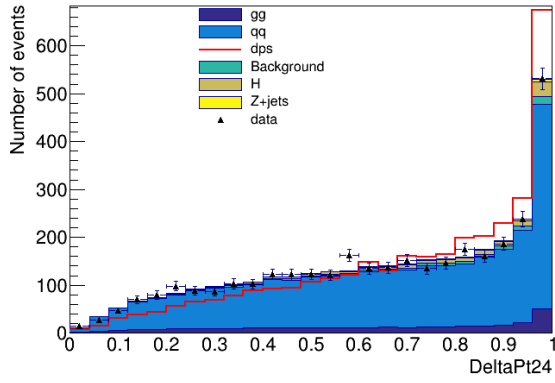
(b) DeltaPt13



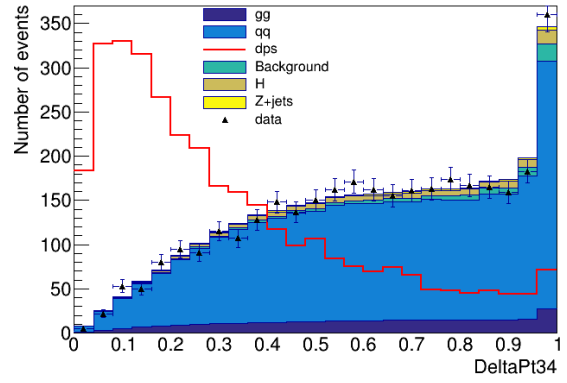
(c) DeltaPt14



(d) DeltaPt23

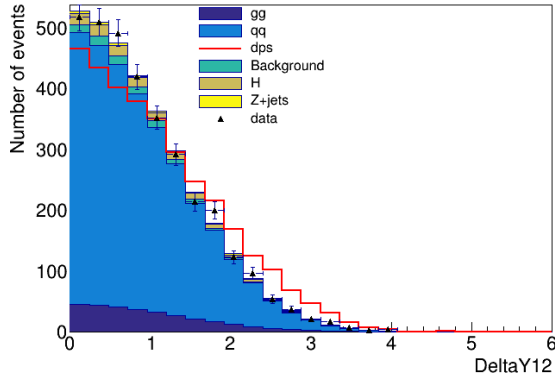


(e) DeltaPt24

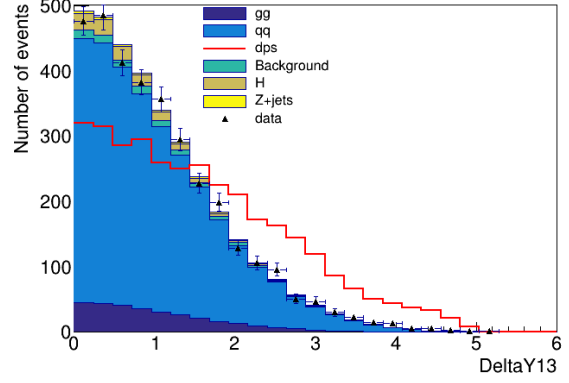


(f) DeltaPt34

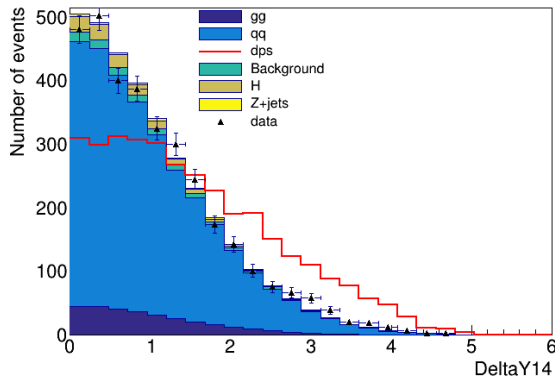
Figure 7.4: Distributions of the ΔP_T for any two leptons



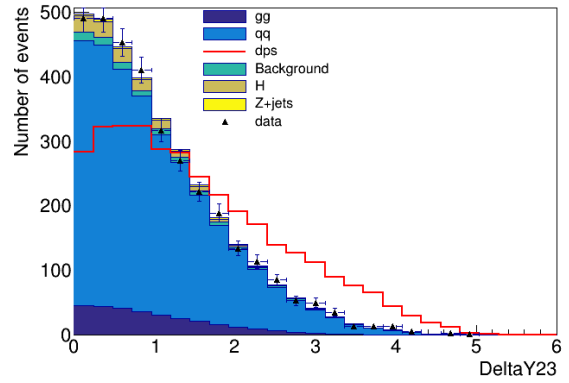
(a) DeltaY12



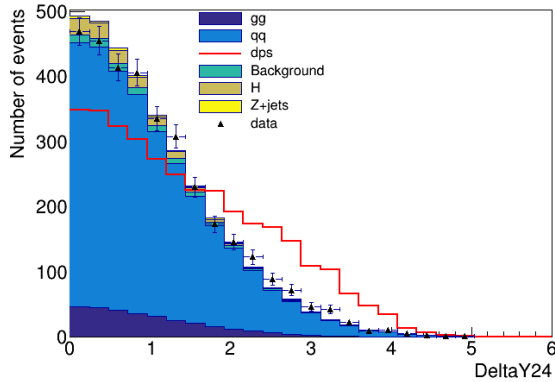
(b) DeltaY13



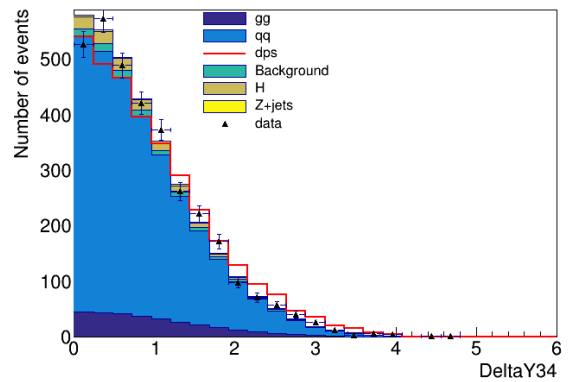
(c) DeltaY14



(d) DeltaY23



(e) DeltaY24



(f) DeltaY34

Figure 7.5: Distribution of the rapidity difference between any two leptons

7.2 DPS Estimation Method

The fraction of DPS events in the data was estimated by fitting the output of an artificial neural network (NN) on the data and MC. The neural network was trained on

distinguishing DPS events from SPS events using the discriminating variables that are presented in Section 7.1. The NN method was chosen in order to utilize any correlations between the discriminating variables that might have been overlooked otherwise. There were 2 hidden layers with 14 and 7 neurons between the input and the output. The input included the 21 discriminating variables and the output was a single neuron with the meaning of "probability to be DPS". The training was done with the Broyden-Fletcher-Goldfarb-Shanno method using approximately 50k events from the DPS sample, 15k events from Z+jets simulation and a composition of 200k events of all other SPS. Z+jets events are poorly recognized by a network trained with other SPS. Therefore, they were given a bigger weight in the training of the NN. The different processes in the SPS (excluding Z+jets) were weighted to their relative contribution in the invariant 4 lepton mass histogram. Half of the events were used for training and half for testing. In the calculation of the error function the DPS, SPS and Z+jets events were separately weighted to 100k events, which guaranteed that they all had a similar significance in the training.

To monitor the learning rate of the NN, it was trained with a different amount of statistics, and the resulting error functions were compared. The considered statistics configurations included:

- SPS:500k DPS:100k
- SPS:300k DPS:75k
- SPS:200k DPS:50k

Each network was trained for 3000 epochs. For all cases the network didn't converge and the rate of improvement of the error functions was identical. This exercise showed that there is no noticeable gain in using all the available statistics, which led to the choice of taking all available events in the Z+jets simulations and the above mentioned SPS and DPS samples.

To check the competency of the chosen NN structure, a more complicated NN with 32 and 14 neurons in the hidden layers was examined and compared to the smaller NN using a purity versus efficiency plot in Figure 7.6. The gain in efficiency was compromised for a shorter training time.

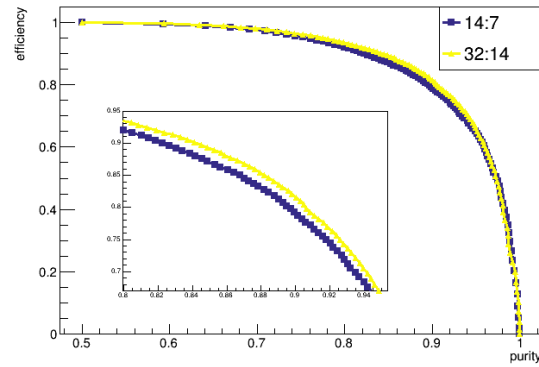


Figure 7.6: Purity vs. efficiency plot for two NN trained using the same statistics. One with 32 neurons in the first layer and 14 in the second layer, the other with 14 neurons in the first layer and 7 in the second layer. The bigger NN gave a better efficiency, especially for purity values around 85%.

The NN was trained for 1200 epochs. Every 100 epochs the NN was saved. The choice with the smallest error function was selected. The results of the NN training are shown in Figure 7.7. The selected stopping point of the training was at 900 epochs, where the error function of the testing sample stopped improving.

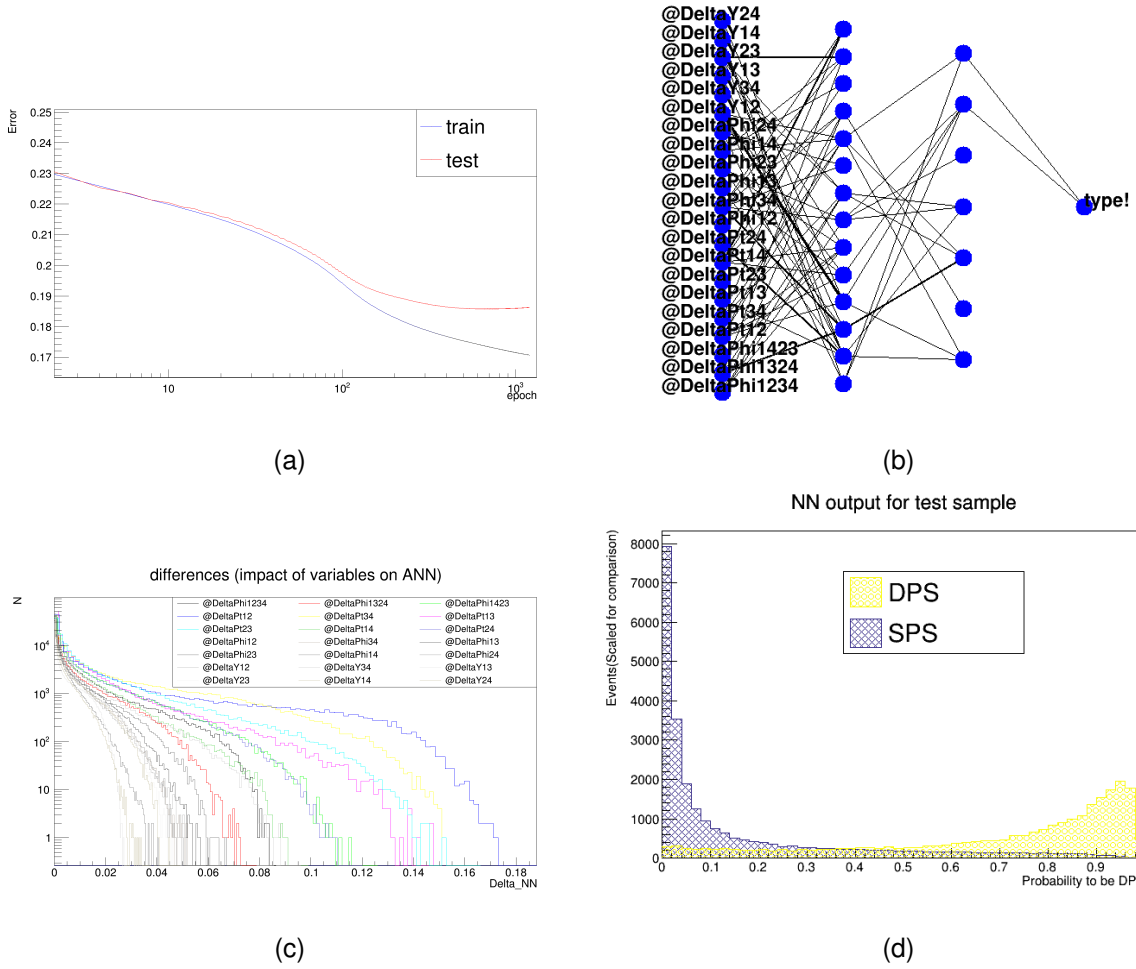


Figure 7.7: The resulting NN after taking the weights at the 900 epoch of training with the selected structure and statistics. 7.7(a) shows the profile of the error function on both the train and the test samples during the 1200 epochs of training. The train and test samples had the same size, and no normalization was needed for the comparison. The training was stopped at the 900 epoch where the error function of the test sample stopped improving. 7.7(b) is a graphic representation of the NN. Each dot represents a neuron, and a connection between dots corresponds to their weight. Thicker lines represent bigger weights. 7.7(c) is a plot of the variable significance estimation for the NN. Each histogram shows the change in the output of the test sample with the corresponding variable varied up and down by 10% of its RMS [41]. 7.7(d) is the distribution of the trained NN output for the DPS and the SPS in the test sample after they were normalized to the same amount.

7.3 Signal Extraction

The resulting NN was used to get the distribution of the DPS probability in the data, SPS and DPS. All samples were converted to histograms with 20 equidistant bins in the range $[0, 1]$. The SPS and DPS output histograms were normalized to the data histogram after SPS-background subtraction. The predicted distribution of the data was taken to be:

$$H_{predicted} = f_{DPS} H_{DPS \text{ normalized}} + (1 - f_{DPS}) H_{SPS \text{ normalized}} + H_{Background} \quad (7.1)$$

where H_{sample} is the histogram of the NN output for the relevant sample, and f_{DPS} is the estimated fraction of the DPS processes. Both DPS and SPS samples were normalized to data minus background. To find the fraction, the likelihood function, calculated according to equation (7.2), was maximized

$$L(f_{DPS}) = \prod_i \frac{(n_i^{predicted})^{n_i^{data}}}{n_i^{data}} \exp^{-n_i^{predicted}} \quad (7.2)$$

Here L is the likelihood (LH) function, n_i is the number of events in bin i in the histogram of the relevant distribution of the NN output. The optimization was done in MINUIT using MIGRAD algorithm [42, 43]. When an error estimation was needed, it was calculated using HESSE algorithm with the error defined as the step size that makes a difference of 0.5 in the LH from (7.2). This method assumes that there is only statistical uncertainty in the data, and the MC uncertainty is neglected.

In order to get an estimate for the DPS fraction that also takes into account the systematic uncertainties of the MC samples, the normalization of the MC samples in the LH function in (7.2) were allowed to change, introducing another 9 degrees of freedom to the minimization. In order to restrict the change of the normalization to the uncertainty of each MC, the LH was also multiplied by Gaussian probability distribution functions:

$$L_2(f_{DPS}, \vec{x}) = L(f_{DPS}) \prod_i \text{Gaussian}(x_i - \alpha_i, \sigma_i) \quad (7.3)$$

where x_i is the amplitude of the i process, α_i is the corresponding estimated normalization and σ_i is the corresponding total uncertainty.

Additional analysis was performed in order to check the uncertainty of the DPS fraction in the experiment. A sample of 5000 pseudo experiments was generated, each

with a randomly generated normalization for the MC processes. The normalization of each process had a Gaussian distribution with the nominal value as the mean and the total uncertainty as the width. The DPS fraction was calculated for each of these experiments by minimizing the LH as per (7.2). This method was expected to give an estimate to the DPS fraction while considering only the MC uncertainties.

7.4 Sigma Effective

The σ_{eff} was calculated using the "pocket" formula in (2.3). Estimation for the cross section of the DPS was obtained using $\sigma_{DPS} = f_{DPS}\sigma_{4l}$, where σ_{4l} was the cross section of the observed events. The cross section of the DY, for calculating $\sigma_{SPS}^{A/B}$ in (2.3), was obtained from the generated DY MC, without taking into account the actual measurements of this process in the experiment. To justify that, it was confirmed that the simulated DY gave a reasonable description of the data in the experiment.

One method for estimating the value of $\frac{1}{1+\delta}$ was to assume that the phase space of the leading Z boson B is contained in the phase space of the sub-leading Z boson A. Then, following the calculations in [41], a symmetry factor γ can be defined so that:

$$\gamma = \frac{\sigma_{SPS}^B}{\sigma_{SPS}^A}, \frac{1}{1+\delta} = 1 - \frac{\gamma}{2} \quad (7.4)$$

However, the phase-spaces of the DY for the leading and sub-leading Z bosons aren't necessarily contained in one another because the pairing of the leptons to dileptons in the DPS quads might mix leptons between different DY events. Therefore, to get the effect of the δ in (2.3) correctly, the multiplication of the DY cross sections was performed event-by-event using:

$$\frac{1}{1+\delta}\sigma_{DY}^1\sigma_{DY}^2 = \sum_{events} \left(\frac{1}{L_{DY}}\right)^2 s_{event} \quad (7.5)$$

where L_{DY} is the luminosity of the sample, and s_{event} is $\frac{1}{2}$ for events with indistinguishable dileptons in a common phase space, 0 for events outside selection and 1 otherwise. This calculation followed the one done in [39]. The DY sample was divided to regions by the following rules:

- The lepton with the higher P_T was separated into: lower than 10 GeV, between 10 to 15, between 15 to 20 and above 20.

- Similar separation was done for the lepton with the lower P_T
- Di-lepton mass was separated into: between 12 and 50 GeV, and between 50 and 120 GeV . and the rest.
- Di-lepton flavor was separated into electrons and muons

The calculation in (7.5) was done for each combination of two regions. This study was performed on 50k DY events. Events with more than 2 leptons were filtered out of the sample. The calculation resulted in $\frac{1}{1+\delta}\sigma_{DY}^1\sigma_{DY}^2 = 4.989 \pm 0.078 nb^2$.

Chapter 8

Results and Conclusions

The nominal result for the DPS fraction, which was retrieved from maximizing (7.2) and includes only the statistical uncertainty of the data:

$$f_{DPS}^{fixedMC} = 0.0209 \pm 0.0075 \quad (8.1)$$

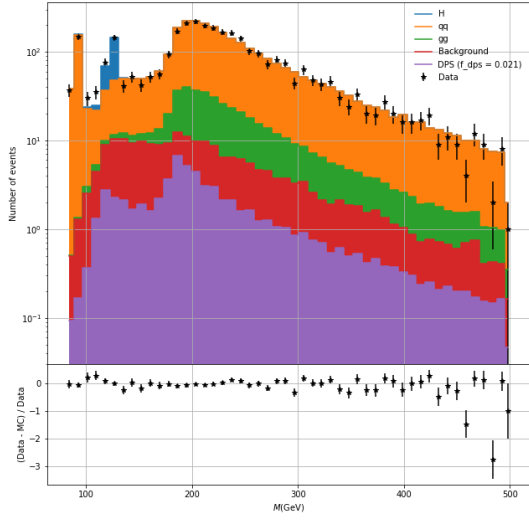
This corresponds to 70 ± 25 DPS events in the data sample.

The results for the DPS fraction and event numbers for the LH where the normalization of the simulated processes were allowed to vary is given in Table 8. The resulting DPS fraction from the table corresponds to 64 ± 28 DPS events in the data sample. This result takes into account both the statistical uncertainty of the data and the total uncertainty of the MC.

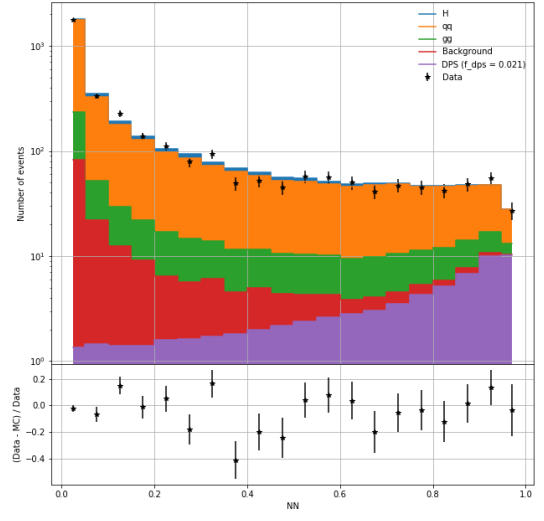
Table 8.1: Results of maximizing (7.3). Other than the DPS fraction, this maximization estimated additionally an expected amount of events for the SPS processes that would better fit the data without contradicting the expectations in Chapter 6.

Parameter	Value
f_{DPS}	0.019 ± 0.0084
gg normalization	410.0 ± 210.0
$q\bar{q}$ normalization	2590.0 ± 340.0
$q\bar{q} + jj$ normalization	30.8 ± 3.9
H normalization	138.0 ± 17.0
VVV normalization	17.1 ± 2.2
WZ normalization	10.1 ± 1.4
$Z + Jets$ normalization	44.0 ± 19.0
$t\bar{t}$ normalization	27.4 ± 4.3
$t\bar{t}V$ normalization	55.2 ± 6.9

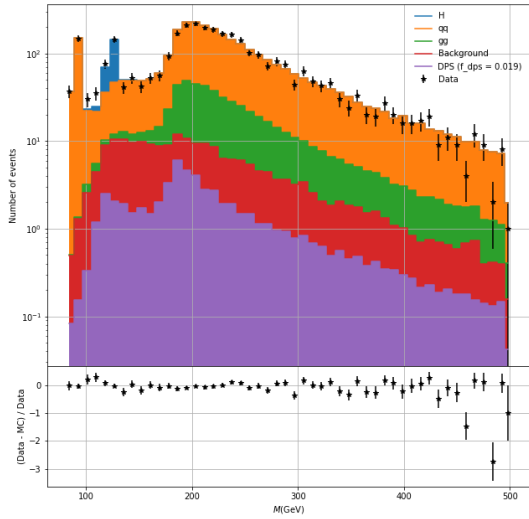
The comparison of the data to MC after the optimizations for both the NN output and the invariant four lepton mass is presented in Figure 8.1.



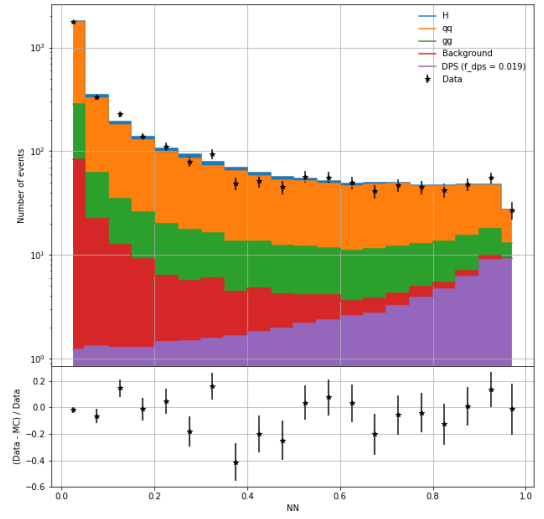
(a) M_{4l} from the maximization of (7.2)



(b) NN output from the maximization of (7.2)



(c) M_{4l} from the maximization of (7.3)



(d) NN output from the maximization of (7.3)

Figure 8.1: Distributions of the NN output and invariant mass of the data and MC after fitting. 8.1(a) and 8.1(b) present the results from maximizing (7.2). 8.1(c) and 8.1(d) present the results from maximizing (7.3).

The resulting DPS fractions from the pseudo experiments are shown in Figure 8.2. For (7.2), the goodness-of-fit, χ^2 , and the number of degrees of freedom of the fit (NDOF) yielded:

$$\chi^2/NDOF = 1.4, P - value = 0.13 \quad (8.2)$$

and for (7.3)

$$\chi^2/NDOF = 0.98, P - value = 0.51 \quad (8.3)$$

For both cases it means that the observation agrees with the prediction at 95% confidence level.

Fitting the distribution of the DPS fraction retrieved from the pseudo experiment to a normal distribution yields:

$$f_{DPS}^{pseudo} = 0.0212 \pm 0.0046 \quad (8.4)$$

The result in (8.4) reassures that the uncertainty of the measurement originating from the statistical uncertainty of the data is larger than the uncertainty originating from the systematic uncertainty of the MC samples. The DPS fraction distribution in the pseudo experiments is presented in Figure 8.2.

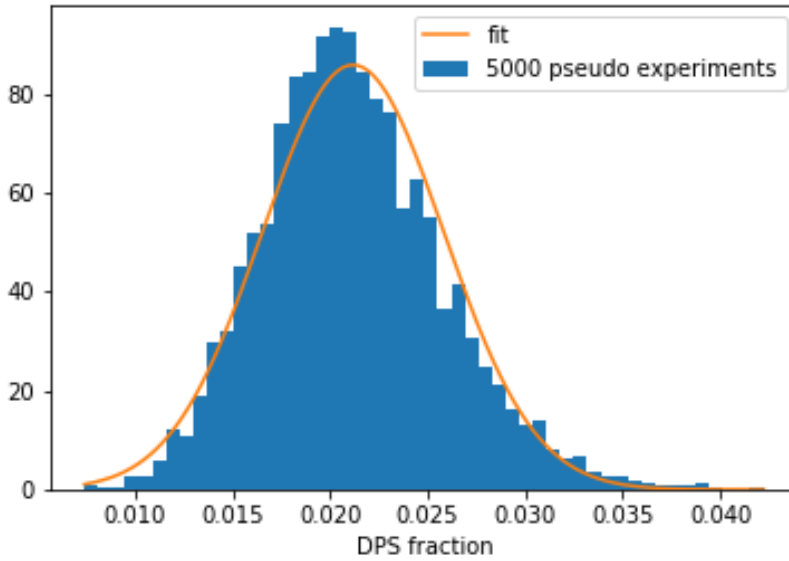


Figure 8.2: Distribution of the DPS fraction in the pseudo experiments. The fit is a Maximum Likelihood Estimate of a Gaussian distribution.

Taking the DPS fraction from Table 8 for the calculation of σ_{eff} yields:

$$\sigma_{eff} = 6.3 \pm 2.9 \text{ mb} \quad (8.5)$$

8.1 Conclusions

The fraction of DPS events in the four lepton channel was measured. The leptons originated from two $Z^{(*)}$ boson decay. The measurement was performed on the data collected in the ATLAS experiment during 2015-2017 and its corresponding MC simulation. The collected data consisted of 80 fb^{-1} of proton-proton collisions at a center of mass energy of $\sqrt{s} = 13 \text{ TeV}$. Out of all the measured events in the experiment, a sample of 3363 events with the required final state were selected. A sample of DPS events was constructed by overlaying DY simulated events. A NN was trained to distinguish between the topology of DPS and SPS events. The DPS fraction was estimated by fitting the output of the NN for the data to the output of the NN for the MC samples of SPS and DPS.

The fraction of double parton scattering in four-lepton events was estimated to be $f_{DPS} = 0.019 \pm 0.0084$. The effective overlap area between the interacting proton was estimated to be $\sigma_{eff} = 6.3 \pm 2.9 \text{ mb}$.

This measurement of the DPS fraction in this study is more significant than the previous measurement of DPS in the same channel for lower center-of-mass. It shows that the contribution of the DPS is not negligible for measurements in higher energies in the four lepton channel. The resulting σ_{eff} is lower than the typical value of 15 mb measured in most of the previous studies from Figure 2.2. However, the result is similar to the previous measurements in channels dominated by $q\bar{q}$ initiated interactions, which further strengthen the assumption that DPS is not universal for all parton combinations.

Appendices

Appendix A

Map of MC Processes to ATLAS Names

Table A.1: The names of the SPS MC files used in the study with their reference index in ATLAS. Each process had two files, one for MC simulation of the 2015-2016 data, and another for the simulation of the 2017 data. The "HIGG2D1.DDOA" version of these files were used. This means the events inside were already filtered with the pre-selection as described in Chapter 4.

Process	ATLAS Name	ATLAS ID
gg	Powheggg2vvPythia8EvtGen_gg_ZZ_bkg_4l_noTau_13TeV	343213
	Powheggg2vvPythia8EvtGen_gg_ZZ_bkg_2e2mu_13TeV	343212
H	PowhegPythia8EvtGen_NNPdf30_AZNLO_ZH125J_Zincl_MINLO	345038
	PowhegPy8EG_NNPdf30_AZNLOCTEQ6L1_VBFH125_ZZ4lep_notau	344235
	PowhegPythia8EvtGen_NNLOPS_nnlo_30_ggH125_ZZ4l	345060
	PowhegPy8EG_A14NNPDF23_NNPdf30ME_ttH125_ZZ4l_allhad_Winc	345936
	PowhegPythia8EvtGen_NNPdf30_AZNLO_WpH125J_Wincl_MINLO	345039
	PowhegPythia8EvtGen_NNPdf30_AZNLO_WmH125J_Wincl_MINLO	345040
	PowhegPythia8EvtGen_A14NNPDF23_NNPdf30ME_ttH125_ZZ4l_dilep	345048
	PowhegPythia8EvtGen_A14NNPDF23_NNPdf30ME_ttH125_ZZ4l_semilep	345047
$q\bar{q}$	PowhegPy8EG_CT10nloME_AZNLOCTEQ6L1_ZZllll_mll4	361603
	Sherpa_222_NNPdf30NNLO_IIIjj_EW6_noHiggs	364364
$t\bar{t}$	PhPy8EG_A14_ttbar_hdamp258p75_dil	410472
	aMcAtNloPythia8EvtGen_MEN30NLO_A14N23LO_ttmumu	410219
	aMcAtNloPythia8EvtGen_MEN30NLO_A14N23LO_ttee	410218
VVV	Sherpa_222_NNPdf30NNLO_ZZZ_4l2v_EW6	364248
	Sherpa_222_NNPdf30NNLO_WZZ_5l1v_EW6	364245
	Sherpa_222_NNPdf30NNLO_ZZZ_6l0v_EW6	364247
	Sherpa_222_NNPdf30NNLO_WWZ_4l2v_EW6	364243
WZ	PowhegPy8EG_CT10nloME_AZNLOCTEQ6L1_WZlvll_mll4	361601
$Z + Jets$	Sherpa_NNPdf30NNLO_Zee_4lMassFilter40GeV8GeV	344295
	Sherpa_NNPdf30NNLO_Zmumu_4lMassFilter40GeV8GeV	344296

Table A.2: The names of the DY MC files used in the study, with their reference index in ATLAS. Each process had two files, one for MC simulation of 2015-2016 data, and another for 2017 data.

ATLAS Name	ATLAS ID
PowhegPythia8EvtGen_AZNLOCTEQ6L1_DYmumu_10M60	361667
PowhegPythia8EvtGen_AZNLOCTEQ6L1_Zmumu	361107
PowhegPythia8EvtGen_AZNLOCTEQ6L1_DYmumu_120M180	301020
PowhegPythia8EvtGen_AZNLOCTEQ6L1_DYmumu_180M250	301021
PowhegPythia8EvtGen_AZNLOCTEQ6L1_DYmumu_250M400	301022
PowhegPythia8EvtGen_AZNLOCTEQ6L1_DYee_10M60	361665
PowhegPythia8EvtGen_AZNLOCTEQ6L1_Zee	361106
PowhegPythia8EvtGen_AZNLOCTEQ6L1_DYmumu_120M180	301020
PowhegPythia8EvtGen_AZNLOCTEQ6L1_DYmumu_180M250	301021
PowhegPythia8EvtGen_AZNLOCTEQ6L1_DYee_250M400	301002

Appendix B

Detector Calibration Systematic Uncertainties

All the systematic uncertainties in the analysis associated with the experimental measurements were calculated by repeating the analysis with a variation of one of the Nuisance Parameters (NP). The list of all the NPs in the experiment is available in Tables B.1 and B.2. Unfortunately, in this study, all the variations for all the available NPs systematically decreased the value of the resulting DPS fraction, indicating an existence of some error in the repetitions of the analysis with the varied NPs. However, the effect of the variations on the final result, even though they had an unexplained bias, was negligible compared to its uncertainty, as can be seen in Figure B.1. Moreover, the previous analysis with a similar selection [39] showed that the resulting uncertainty is small compared to the theoretical and statistical uncertainties. Therefore, the estimation of these uncertainties was not included in the final results.

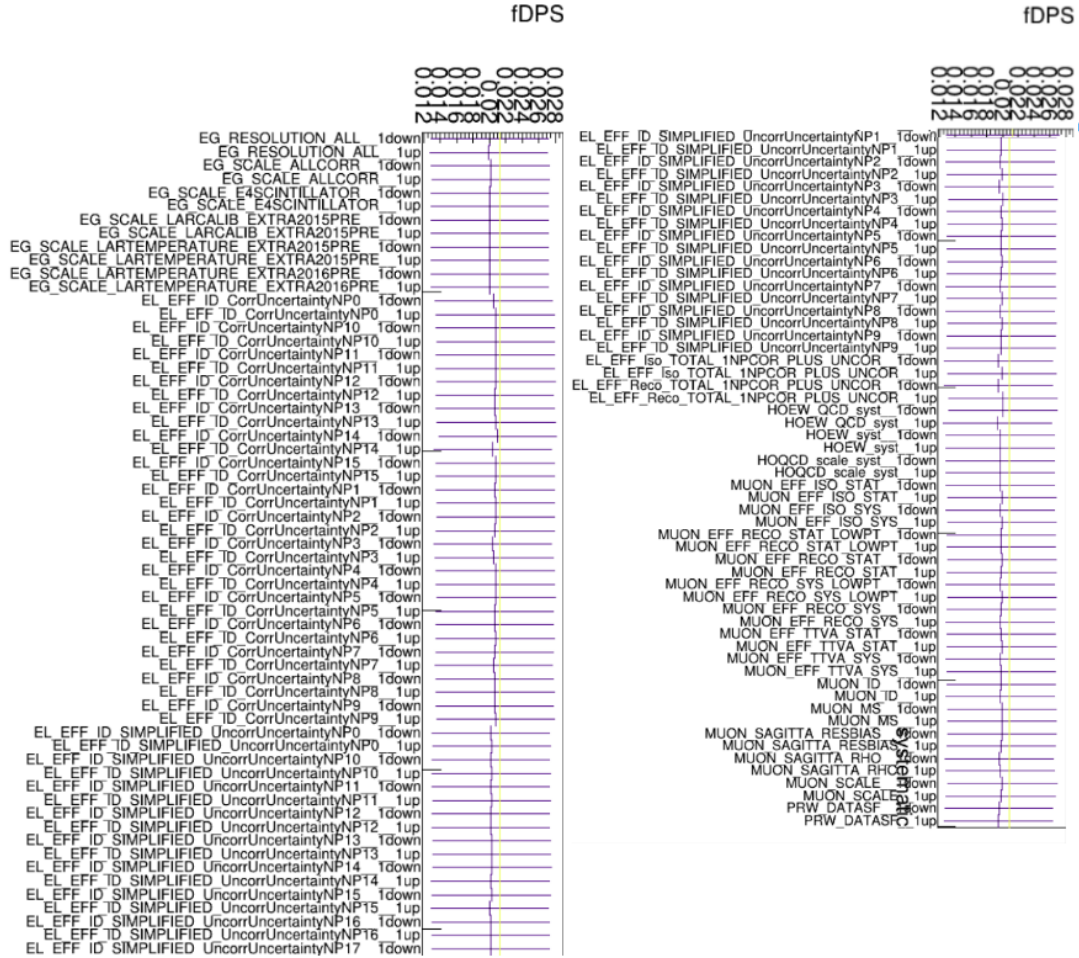


Figure B.1: The results of the analysis with varied nuisance parameters. The yellow line shows the nominal result.

Table B.1: List of the Nuisance Parameters in the Experiment: Part 1

Electron reconstruction and identification	EL_EFF_ID_CorrUncertaintyNP[0-15]
	EL_EFF_ID_SIMPLIFIED_UncorrUncertaintyNP[0-17]
	EL_EFF_Reco_TOTAL_1NPCOR_PLUS_UNCOR
Electron energy scale and resolution	EG_RESOLUTION_ALL
	EG_SCALE_ALLCORR
	EG_SCALE_E4SCINTILLATOR
	EG_SCALE_LARCALIB_EXTRA2015PRE
	EG_SCALE_LARTEMPERATURE_EXTRA2015PRE
	EG_SCALE_LARTEMPERATURE_EXTRA2016PRE
Muon reconstruction and identification	MUON_EFF_RECO_STAT
	MUON_EFF_RECO_STAT_LOWPT
	MUON_EFF_RECO_SYS
	MUON_EFF_RECO_SYS_LOWPT
Muon momentum scale and resolution	MUON_ID
	MUON_MS
	MUON_SCALE
	MUON_SAGITTA_RESBIAS
	MUON_SAGITTA_RHO
Muon track-to-vertex-association (TTVA)	MUON_EFF_TTVA_STAT
	MUON_EFF_TTVA_SYS

Table B.2: List of the Nuisance Parameters in the Experiment: Part 2

Isolation	MUON_EFF_ISO_STAT
	MUON_EFF_ISO_SYS
	EL_EFF_Iso_TOTAL_1NPCOR_PLUS_UNCOR
Jet energy scale	JET_EffectiveNP_[1-7]
	JET_EffectiveNP_8restTerm
	JET_EtaIntercalibration_Modelling
	JET_EtaIntercalibration_NonClosure_highE
	JET_EtaIntercalibration_NonClosure_negEta
	JET_EtaIntercalibration_NonClosure_posEta
	JET_EtaIntercalibration_TotalStat
	JET_PunchThrough_MC16
	JET_SingleParticle_HighPt
	JET_Flavor_Composition
	JET_Flavor_Response
	JET_BJES_Response
Jet energy resolution	JET_JER_SINGLE_NP(varied only up)
Flavour tagging	FT_EFF_Eigen_B_[0-2]
	FT_EFF_Eigen_C_[0-2]
	FT_EFF_Eigen_Light_[0-4]
	FT_EFF_extrapolation

Bibliography

- [1] G. Aad *et al.*, “Observation of a new particle in the search for the Standard Model Higgs boson with the ATLAS detector at the LHC,” *Phys. Lett.*, vol. B716, pp. 1–29, 2012.
- [2] S. Chatrchyan *et al.*, “Observation of a new boson at a mass of 125 GeV with the CMS experiment at the LHC,” *Phys. Lett.*, vol. B716, pp. 30–61, 2012.
- [3] H. Baer, T. Barklow, K. Fujii, Y. Gao, A. Hoang, S. Kanemura, J. List, H. E. Logan, A. Nomerotski, M. Perelstein, *et al.*, “The International Linear Collider Technical Design Report - Volume 2: Physics,” 2013.
- [4] G. Aad *et al.*, “The ATLAS Experiment at the CERN Large Hadron Collider,” *JINST*, vol. 3, p. S08003, 2008.
- [5] S. Chatrchyan *et al.*, “The CMS Experiment at the CERN LHC,” *JINST*, vol. 3, p. S08004, 2008.
- [6] N. Paver and D. Treleani, “MULTIPLE PARTON PROCESSES IN THE TeV REGION,” *Z. Phys. C*, vol. 28, p. 187, 1985.
- [7] M. Diehl, “Multiparton interactions: Theory and experimental findings,” 2013.
- [8] B. Blok, Y. Dokshitser, L. Frankfurt, and M. Strikman, “pQCD physics of multiparton interactions,” *Eur. Phys. J. C*, vol. 72, p. 1963, 2012.
- [9] S. D. Drell and T.-M. Yan, “Massive lepton-pair production in hadron-hadron collisions at high energies,” *Phys. Rev. Lett.*, vol. 25, pp. 316–320, Aug 1970.
- [10] C. Goebel, F. Halzen, and D. M. Scott, “Double Drell-Yan Annihilations in Hadron Collisions: Novel Tests of the Constituent Picture,” *Phys. Rev.*, vol. D22, p. 2789, 1980.

- [11] M. Aaboud *et al.*, “Study of the hard double-parton scattering contribution to inclusive four-lepton production in pp collisions at $\sqrt{s} = 8$ TeV with the ATLAS detector,” *Submitted to: Phys. Lett.*, 2018.
- [12] M. W. Krasny and W. Placzek, “The LHC excess of four-lepton events interpreted as Higgs-boson signal: Background from Double Drell-Yan process?,” *Acta Phys. Polon.*, vol. B45, no. 1, pp. 71–87, 2014.
- [13] M. W. Krasny and W. Placzek, “On the contribution of the double Drell-Yan process to WW and ZZ production at the LHC,” *Acta Phys. Polon.*, vol. B47, pp. 1045–1056, 2016.
- [14] G. Aad *et al.*, “Measurements of four-lepton production in pp collisions at $\sqrt{s} = 8$ TeV with the ATLAS detector,” *Phys. Lett.*, vol. B753, pp. 552–572, 2016.
- [15] M. Aaboud *et al.*, “Measurement of the four-lepton invariant mass spectrum in 13 TeV proton-proton collisions with the ATLAS detector,” 2019.
- [16] A. D. Martin, R. G. Roberts, W. J. Stirling, and R. S. Thorne, “Parton distributions: A New global analysis,” *Eur. Phys. J.*, vol. C4, pp. 463–496, 1998.
- [17] J. Gao, M. Guzzi, J. Huston, H.-L. Lai, Z. Li, P. Nadolsky, J. Pumplin, D. Stump, and C. P. Yuan, “CT10 next-to-next-to-leading order global analysis of QCD,” *Phys. Rev.*, vol. D89, no. 3, p. 033009, 2014.
- [18] R. D. Ball *et al.*, “Parton distributions for the LHC Run II,” *JHEP*, vol. 04, p. 040, 2015.
- [19] D. Kyriazopoulos, *Double Drell-Yan measurement, heavy Higgs searches in the four leptons final state and forward muons performance with the ATLAS detector*. PhD thesis, Sheffield U., 2015-12-22.
- [20] ATLAS Collaboration, “The ATLAS Experiment at the CERN Large Hadron Collider,” *JINST*, vol. 3, p. S08003. 437 p, 2008. Also published by CERN Geneva in 2010.
- [21] M. Cano Bret, S. H. Abidi, A. Schaffer, A. Gabrielli, D. Denysiuk, R. Nicolaidou, W. Su, R. F. Naranjo Garcia, W. A. Leight, J. W. Carter, H. Herde, X. Ju, G. Ar-

- toni, J. Meyer, C. Anastopoulos, S. Hassani, G. Barone, R. Di Nardo, B. Haney, S. Heim, M. Goblirsch-Kolb, P. Podberezko, S. E. Von Buddenbrock, T. Lagouri, and L. Xu, “Search for heavy ZZ resonances in the $\ell^+\ell^-\ell^+\ell^-$ final state using proton–proton collisions at $\sqrt{s} = 13$ TeV with the ATLAS detector,” Tech. Rep. ATL-COM-PHYS-2018-1042, CERN, Geneva, Jul 2018.
- [22] T. Gleisberg, S. Hoeche, F. Krauss, M. Schonherr, S. Schumann, F. Siegert, and J. Winter, “Event generation with SHERPA 1.1,” *JHEP*, vol. 02, p. 007, 2009.
- [23] S. Alioli, P. Nason, C. Oleari, and E. Re, “A general framework for implementing NLO calculations in shower Monte Carlo programs: the POWHEG BOX,” *JHEP*, vol. 06, p. 043, 2010.
- [24] T. Sjostrand, S. Mrenna, and P. Z. Skands, “A Brief Introduction to PYTHIA 8.1,” *Comput. Phys. Commun.*, vol. 178, pp. 852–867, 2008.
- [25] “CTEQ.” <http://www.physics.smu.edu/scalise/cteq/>.
- [26] R. D. Ball *et al.*, “Parton distributions with LHC data,” *Nucl. Phys.*, vol. B867, pp. 244–289, 2013.
- [27] G. Aad *et al.*, “Measurement of the Z/γ^* boson transverse momentum distribution in pp collisions at $\sqrt{s} = 7$ TeV with the ATLAS detector,” *JHEP*, vol. 09, p. 145, 2014.
- [28] “ATLAS Run 1 Pythia8 tunes,” Tech. Rep. ATL-PHYS-PUB-2014-021, CERN, Geneva, Nov 2014.
- [29] D. J. Lange, “The EvtGen particle decay simulation package,” *Nucl. Instrum. Meth.*, vol. A462, pp. 152–155, 2001.
- [30] “ggvv.” <https://gg2vv.hepforge.org>.
- [31] J. Alwall, M. Herquet, F. Maltoni, O. Mattelaer, and T. Stelzer, “MadGraph 5 : Going Beyond,” *JHEP*, vol. 06, p. 128, 2011.
- [32] G. Aad *et al.*, “The ATLAS Simulation Infrastructure,” *Eur. Phys. J.*, vol. C70, pp. 823–874, 2010.

- [33] A. Bierweiler, T. Kasprzik, and J. H. Khn, “Vector-boson pair production at the LHC to $\mathcal{O}(\alpha^3)$ accuracy,” *JHEP*, vol. 12, p. 071, 2013.
- [34] F. Cascioli, T. Gehrmann, M. Grazzini, S. Kallweit, P. Maierhofer, A. von Manteuffel, S. Pozzorini, D. Rathlev, L. Tancredi, and E. Weihs, “ZZ production at hadron colliders in NNLO QCD,” *Phys. Lett.*, vol. B735, pp. 311–313, 2014.
- [35] K. Melnikov and M. Dowling, “Production of two Z-bosons in gluon fusion in the heavy top quark approximation,” *Phys. Lett.*, vol. B744, pp. 43–47, 2015.
- [36] S. H. Abidi, C. Anastopoulos, S. Angelidakis, G. Artoni, O. K. Baker, G. Barone, P. Bellos, N. Belyaev, V. Bortolotto, M. Cano Bret, J. Carter, F. Cerutti, G. Cree, T. Cuhadar Donszelmann, T. Dai, D. Denysiuk, R. Di Nardo, D. Divalentino, K. M. Ecker, G. Eigen, D. Fassouliotis, L. Flores Castillo, A. Gabrielli, S. Gargiulo, C. Geng, M. Goblirsch-Kolb, B. Haney, S. Hassani, S. Heim, H. Herde, L. Ikonomidou-Fayard, X. Ju, T. Koffas, R. Konoplich, O. Kortner, S. Kortner, C. Kourkoumelis, T. S. Lau, A. Laudrain, W. A. Leight, A. Lesage, K. Lie, J. Li, H. Lu, N. Lu, G. Mancini, A. Maslennikov, M. McKay, J. Meyer, E. Mountricha, T. Y. Ng, R. Nicolaidou, I. Nomidis, S. Oda, D. Paredes Hernandez, P. Podberezko, K. Potamianos, T. D. Powell, K. Prokofiev, S. Rosati, A. Salvucci, A. Schaffer, G. Sciolla, R. Stroynowski, R. Tanaka, M. Trovatielli, L. M. Veloce, V. M. Walbrecht, R. Wang, H. Williams, S. L. Wu, H. Yang, Z. Yang, Z. Zhao, B. Zhou, and L. Xu, “Event selection and background estimation in the $H \rightarrow ZZ^{(*)} \rightarrow 4\ell$ channel at $\sqrt{s} = 13$ TeV - Moriond 2017 Analysis,” Tech. Rep. ATL-COM-PHYS-2016-1599, CERN, Geneva, Nov 2016.
- [37] G. Artoni, G. Barone, K. M. Loew, H. Herde, G. Sciolla, M. Bellomo, M. Goblirsch-Kolb, N. M. Koehler, M. Sioli, R. Nicolaidou, A. Lesage, D. Zhang, S. Hu, S. Zambito, F. Sforza, M. Gignac, I. Nomidis, P. Kluit, N. van Eldik, J. Meyer, M. Corradi, F. Cardillo, C. Ferretti, E. Diehl, T. Koffas, W. A. Leight, and G. Cree, “Support Note for 2015 Muon Combined Performance Paper ,” Tech. Rep. ATL-COM-PHYS-2015-1149, CERN, Geneva, Sep 2015. Support note for ATL-COM-PHYS-2015-1564.

- [38] M. Tanabashi *et al.*, “Review of Particle Physics,” *Phys. Rev. D*, vol. 98, no. 3, p. 030001, 2018.
- [39] M. Aaboud, G. Aad, B. Abbott, O. Abdinov, B. Abeloos, S. H. Abidi, O. S. AbouZeid, N. L. Abraham, H. Abramowicz, and et al., “Search for heavy ZZ resonances in the $\ell^+\ell^-\ell^+\ell^-$ and $\ell^+\ell^-\nu\bar{\nu}$ final states using proton-proton collisions at $\sqrt{s} = 13$ TeV with the ATLAS detector,” *The European Physical Journal C*, vol. 78, Apr 2018.
- [40] “Study of hard double parton scattering in four-jet events in pp collisions at $\sqrt{s} = 7$ TeV with the ATLAS experiment at the LHC,” Tech. Rep. ATLAS-CONF-2015-058, CERN, Geneva, Nov 2015.
- [41] M. Aaboud *et al.*, “Study of hard double-parton scattering in four-jet events in pp collisions at $\sqrt{s} = 7$ TeV with the ATLAS experiment,” *JHEP*, vol. 11, p. 110, 2016.
- [42] F. James and M. Roos, “Minuit – A System for Function Minimization and Analysis of the Parameter Errors and Correlations,” *Computer Physics Communications*, vol. 10, pp. 343–367, Dec. 1975.
- [43] iminuit team, “iminuit – a python interface to minuit.” <https://github.com/scikit-hep/iminuit>. Accessed: 2018-03-05.